The Astrophysical Journal Supplement Series, 246:66 (18pp), 2020 February https://doi.org/10.3847/1538-4365/ab6c65

Ion-scale Electromagnetic Waves in the Inner Heliosphere

Trevor A. Bowen[1], Alfred Mallet[1], Jia Huang[2], Kristopher G. Klein[3], David M. Malaspina[4], Michael Stevens[5], Stuart D. Bale[1,6,7,8], J. W. Bonnell[1], Anthony W. Case[5], Benjamin D. G. Chandran[9,10], C. C. Chaston[1], Christopher H. K. Chen[8], Thierry Dudok de Wit[11], Keith Goetz[12], Peter R. Harvey[1], Gregory G. Howes[13], J. C. Kasper[2,5], Kelly E. Korreck[5], Davin Larson[1], Roberto Livi[1], Robert J. MacDowall[14], Michael D. McManus[1,6], Marc Pulupa[1], J. L. Verniero[1], and Phyllis Whittlesey[1]
(The PSP/FIELDS and PSP/SWEAP Teams)
[1] Space Sciences Laboratory, University of California, Berkeley, CA 94720-7450, USA; tbowen@berkeley.edu
[2] Climate and Space Sciences and Engineering, University of Michigan, Ann Arbor, MI 48109, USA
[3] University of Arizona, Tucson, AZ, USA
[4] Laboratory for Atmospheric and Space Physics, University of Colorado, Boulder, CO 80303, USA
[5] Smithsonian Astrophysical Observatory, Cambridge, MA 02138, USA
[6] Physics Department, University of California, Berkeley, CA 94720-7300, USA
[7] The Blackett Laboratory, Imperial College London, London, SW7 2AZ, UK
[8] School of Physics and Astronomy, Queen Mary University of London, London E1 4NS, UK
[9] Department of Physics & Astronomy, University of New Hampshire, Durham, NH 03824, USA
[10] Space Science Center, University of New Hampshire, Durham, NH 03824, USA
[11] LPC2E, CNRS and University of Orléans, Orléans, France
[12] School of Physics and Astronomy, University of Minnesota, Minneapolis, MN 55455, USA
[13] Department of Physics and Astronomy, University of Iowa, Iowa City, IA 52242, USA
[14] Solar System Exploration Division, NASA/Goddard Space Flight Center, Greenbelt, MD 20771, USA
Received 2019 September 17; revised 2020 January 13; accepted 2020 January 14; published 2020 February 6

Abstract

Understanding the physical processes in the solar wind and corona that actively contribute to heating, acceleration, and dissipation is a primary objective of NASA's *Parker Solar Probe* (*PSP*) mission. Observations of circularly polarized electromagnetic waves at ion scales suggest that cyclotron resonance and wave–particle interactions are dynamically relevant in the inner heliosphere. A wavelet-based statistical study of circularly polarized events in the first perihelion encounter of *PSP* demonstrates that transverse electromagnetic waves at ion resonant scales are observed in 30–50% of radial field intervals. Average wave amplitudes of approximately 4 nT are measured, while the mean duration of wave events is on the order of 20 s; however, long-duration wave events can exist without interruption on hour-long timescales. Determination of wave vectors suggests propagation parallel/antiparallel to the mean magnetic field. Though ion-scale waves are preferentially observed during intervals with a radial mean magnetic field, we show that measurement constraints, associated with single spacecraft sampling of quasi-parallel waves superposed with anisotropic turbulence, render the measured coherent ion-wave spectrum unobservable when the mean magnetic field is oblique to the solar wind flow; these results imply that the occurrence of coherent ion-scale waves is not limited to a radial field configuration. The lack of radial scaling of characteristic wave amplitudes and duration suggests that the waves are generated in situ through plasma instabilities. Additionally, observations of proton distribution functions indicate that temperature anisotropy may drive the observed ion-scale waves.

Unified Astronomy Thesaurus concepts: Solar wind (1534); Space plasmas (1544); Solar coronal heating (1989); Interplanetary turbulence (830); Plasma astrophysics (1261)

1. Introduction

The collisionless nature of the solar wind suggests that wave–particle interactions are necessary for the dissipation of magnetized turbulence. The ion-cyclotron resonance, which enables coupling of electromagnetic fluctuations with ion gyromotion (e.g., Stix 1992), may contribute to coronal heating through damping of Alfvénic fluctuations at ion gyroscales (Hollweg & Johnson 1988; Tu & Marsch 1997; Cranmer 2000, 2014). Measurements of ion temperature anisotropies in the upper corona by ultraviolet spectroscopy suggest large $T_\perp/T_\parallel$ consistent with heating through cyclotron damping (Kohl et al. 1997, 1998; Cranmer et al. 1999; Cranmer 2000).

In the solar wind, observations of nonzero magnetic helicity at ion scales have been interpreted as evidence for active cyclotron damping of turbulent fluctuations, which contribute to the dissipation and heating at kinetic scales (Isenberg 1990; Leamon et al. 1998; Woodham et al. 2018). In addition to proton–cyclotron dynamics, the cyclotron resonance of doubly ionized helium (α-particles) and heavy ions has been studied extensively (Isenberg & Hollweg 1983; Isenberg 1984). Using observations of protons and α-particles, Kasper et al. (2013) argue that temperature anisotropy observed at 1 au is consistent with in situ cyclotron resonant heating—though alternative theories may produce consistent solutions with other dissipation mechanisms, e.g., stochastic heating (Chandran et al. 2013).

Observational studies of magnetic helicity of the solar wind by Podesta & Gary (2011a) and He et al. (2011) reveal circular polarized fluctuations near the proton gyroscale, $\rho = V_{\perp \mathrm{pth}}/\Omega_p$, where $V_{\perp \mathrm{pth}}$ is the proton thermal speed perpendicular to the mean magnetic field, $\boldsymbol{B}_0$, and $\Omega_p = qB_0/m_p$. Both studies found opposite polarizations at $|\cos\theta_{\mathrm{BV}}| \approx 1$ and $|\cos\theta_{\mathrm{BV}}| \approx 0$,

where θ_{BV} is the angle between the mean magnetic field and the solar wind flow direction. Podesta & Gary (2011a) suggest that the observations are consistent with parallel propagating ion-cyclotron wave (ICWs) or fast-magnetosonic/whistler (FM/W) waves and anisotropic kinetic Alfénic turbulence. He et al. (2011) interpret the observations as the result of a parallel propagating ICW population and oblique FM/W population.

Podesta & Gary (2011b) demonstrate the generation of ICW waves propagating anti-sunward and electron-resonant FM/W waves propagating Sunward from through the respective Alfén/ion cyclotron and parallel firehose instabilities; the authors further argue that the Doppler shift of sunward-propagating electron waves causes both modes to appear ion-resonant in the spacecraft frame. Klein et al. (2014) reproduced the observations of helicity by Podesta & Gary (2011a) and He et al. (2011) using a superposition of quasi-perpendicular Alfvénic turbulence with quasi-parallel propagating ICWs and electron resonant whistler waves, concluding that measurements of helicity alone are not sufficient to distinguish the wave modes. Using a *k*-filtering technique, Roberts & Li (2015) determined that observed wave vectors were consistent with ion-resonant fluctuations rather than an FM/W mode.

While observations of the spectrum parallel to the magnetic field ($k_{\|}$) at kinetic scales suggest the presence of background fluctuations with an intrinsic nonzero helicity, ion-scale waves with coherent circular polarization have been observed in many space-plasma environments. Observations of ICWs near planetary bodies are commonly associated with pick up of ions from neutral atmospheres (Russell et al. 1990; Kivelson et al. 1996; Brain et al. 2002; Delva et al. 2011). Using ISEE-3 magnetometer data, Tsurutani et al. (1994) observed elliptically polarized ion-scale waves upstream of the Earth with several nT amplitudes on the order of the mean field strength. Though the authors conjectured that the waves result from pickup-ion interaction, they could not rule out generation through instabilities or a solar source. (Murphy et al. 1995) noted that the presence of circularly polarized ion-scale waves in *Ulysses* observations occurred preferentially with a radial field alignment; their observations, spanning roughly two years and taken far from planetary sources, led the authors to conclude that interstellar pickup ion interactions were the source of these waves.

Using the twin *STEREO* spacecraft spacecraft, Jian et al. (2009) performed a statistical study of ion-waves at 1 au spanning two months, identifying both left- and right-hand circular polarizations in the spacecraft frame with amplitudes on the order of 0.1 nT. The two-month interval studied in Jian et al. (2009) coincides with an orbital configuration that precludes planetary generation from Earth and sufficient orbital separation such that observations of ion-scale waves in each satellite could be taken independent events; their results showed that the presence of ICWs preferentially coincides with intervals of radial field, in agreement with the results of Murphy et al. (1995). Subsequent work has revealed the presence of ICWs in the inner heliosphere with both *MESSENGER* and *Helios* data, again with a preference for radial field alignment (Jian et al. 2010). Boardsen et al. (2015) performed a multiyear analysis of frequency wave storms using *MESSENGER* observations. The radial scaling of cyclotron polarized waves was found to be $\sim r^{-3}$, consistent with a WKB-like propagation suggested by Hollweg (1974), leading the authors to argue for the propagation of ICWs from the inner heliosphere. Jian et al. (2014) performed a statistical study of one year of *STEREO* data, comparing the occurrence of long-duration ion-wave events; their results attempt to rule out generation from interstellar pickup or transient solar wind features (shocks, coronal mass ejections), suggesting that the waves may grow through plasma instabilities.

The relatively weak collisionality of the hot and diffuse solar wind allows for the persistence of non-Maxwellian velocity distribution functions, which are typically parameterized by unequal temperatures along and transverse to the local magnetic field direction and distinct particle populations drifting with respect to one another. Both temperature anisotropy and drifting particle populations are commonly measured in the inner heliosphere and at 1 au (Marsch et al. 1982; Cranmer et al. 1999; Marsch 2012; Kasper et al. 2017; Wilson et al. 2018). These non-Maxwellian features are capable of generating coherent waves through quasi-linear processes (Gary 1993; Gary et al. 2001; Kasper et al. 2002; Verscharen et al. 2016, 2019). The unstable waves can be driven by resonant wave–particle interactions, generating a number of different wave modes depending on the local plasma conditions; see Gary (1993) for a classic reference on these unstable modes, and Yoon (2017) for a discussion of their quasi-linear evolution. A number of different kinds of nonequilibrium structures can drive ICWs (e.g., see Table 4 in Verscharen et al. (2019) and references therein) including proton and minor ion temperature anisotropies with $T_{\perp} > T_{\|}$ and relatively drifting ion populations. The conditions for these resonant instabilities, which have their fastest growing modes at wave vectors $k_{\|}\rho \approx 1$ and $k_{\perp} \ll k_{\|}$, arise frequently in the solar wind (Klein et al. 2018).

Several studies have provided observational support for wave generation through instabilities. Wicks et al. (2016) demonstrate correlations between plasma beam energy and coherent wave power, as well as the coincidence of unstable distributions with the presence of long-duration events, interpreting the observations as generation of coherent waves through an anisotropic core-beam instabilities. Separately, Woodham et al. (2019) and Zhao et al. (2019) demonstrate increased occurrence of coherent waves when temperature anisotropy threshold conditions are met.

This manuscript reports detailed measurements of ion-scale waves observed by NASA's *Parker Solar Probe* (*PSP*; Bale et al. 2019). The presence of polarized waves near ion-kinetic scales and the inherent connection of these waves with kinetic instabilities suggest that ion-cyclotron resonance may play a role in coronal heating heating and solar wind acceleration. Furthermore, the ubiquity of transverse ion waves in the inner heliosphere, in comparison with 1 au observations, suggest that these waves—and the processes that drive and damp them—will become more prevalent as *PSP* descends into the solar corona. Through studying the statistical in situ signatures of coherent waves in the inner heliosphere with instrumentation provided by the *PSP* electromagnetic FIELDS and Solar Wind Electron, Alpha, Proton (SWEAP) investigations, we aim to demonstrate the importance of these fluctuations to plasma dynamics in the inner heliosphere (Bale et al. 2016; Kasper et al. 2016).

Section 2 outlines the data acquisition, processing, and coherent wave identification and extraction using a continuous

wavelet transform. Section 3 discusses the statistical observations of polarized wave events in the inner heliosphere. Section 4 provides an analysis of sampling biases due to single spacecraft measurements of a multicomponent wave-vector spectra consisting of anisotropic turbulence and parallel propagating waves. Section 5 compares the occurrence of wave events with estimates of proton core temperature anisotropy made through integrated 1D measurements. Section 6 compares the incidence of electrostatic waves with observations of ion-scale waves.

2. Data Processing and Wavelet Analysis

Data are obtained from the first *PSP* perihelion encounter (E1) between 2018 October 31–November 11. Measurements of the solar wind plasma are made by the Solar Wind Electrons Alphas and Protons (*PSP*/SWEAP) investigation (Fox et al. 2016; Kasper et al. 2016). Moments of ion distribution functions measured by the Solar Probe Cup (SPC) are used in evaluating temperature, T_p, solar wind velocity, $\boldsymbol{V}_{\rm sw}$, and density, n_p, over the first perihelion (Case et al. 2020).

The FIELDS instrument suite provides in situ measurements of electromagnetic fluctuations on *PSP* (Bale et al. 2016; Fox et al. 2016). Magnetic field measurements are taken from the FIELDS flux-gate magnetometer (MAG). During E1, sample rates for the MAG vary between 73.242 and 292.969 Sa s^{-1}. Data are downsampled to a uniform rate of 36.621 Sa s^{-1}, enabling uniform sampling over the first encounter while reducing computational loads and keeping the Doppler-shifted ion scales within the bandwidth. A digital anti-aliasing filter is applied to remove power above the downsampled Nyquist frequency (∼18.32 Hz). SPC plasma data are typically sampled at a lower cadence than the MAG (roughly 0.25–1 s). Plasma moments (T_p, n_p and $V_{\rm sw}$) are interpolated on to the 36.621 Sa s^{-1} magnetic field time base. For each time step, the median value of the neighboring 512 samples (approximately 14 s) is taken to remove impulsive noise and nonfinite measurements. Additionally, using integrated observations of 1D distribution functions from SWEAP/SPC, Huang et al. (2019) construct 3D distribution functions with order 10 s cadence, providing estimates of the anisotropic perpendicular and parallel proton thermal velocities $V_{\perp \rm th}$ and $V_{\parallel \rm th}$.

The FIELDS magnetometer suite is sensitive to narrowband coherent noise originating from the spacecraft reaction wheels. In order to minimize effects of the reaction wheels, which may contaminate magnetic field measurements at ion scales, time-dependent wheel rotation rates are identified from spacecraft housekeeping data. Power in the contaminated frequencies is attenuated in the Fourier domain, removing the polarized narrowband spacecraft noise (which can be mistaken as coherent plasma wave power) from the magnetic field data. The Appendix outlines the data processing technique and its impact on the results of the study.

A wavelet transform is performed for each full day of downsampled magnetic field data to obtain a time-frequency decomposition of the observations. The continuous wavelet transform is given as the convolution of a time series with a set of scaled wavelets $\psi(s, \tau)$ normalized to unit energy at each scale:

$$W(s, t) = \sum_{i=0}^{N-1} \psi\left(\frac{t_i - \tau}{s}\right) B(t_i), \tag{1}$$

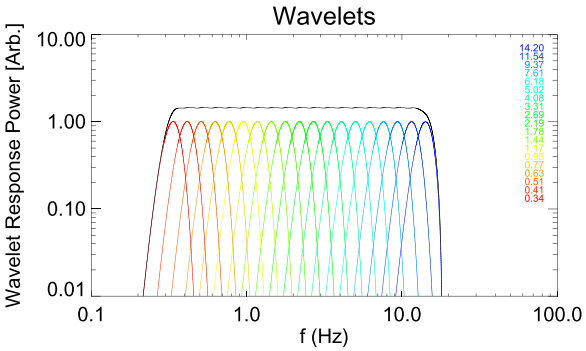

Figure 1. A set of 19 un-normalized Morlet wavelets (Gaussian modulated complex-exponential) with logarithmic spacing between ∼0.34 and 14.20 Hz. The black line shows the integrated response of the set of wavelets over the downsampled (36.621 Sa s^{-1}) MAG bandwidth is uniform.

where the Morlet wavelet, given (in un-normalized form) as

$$\psi(\tau) = \pi^{-1/4} e^{-i\omega_0 \tau} e^{\frac{-\tau^2}{2}}, \tag{2}$$

with nondimensional time and frequency parameters τ and ω_0, is used. (Farge 1992; Torrence & Compo 1998; Dudok de Wit et al. 2013). The continuous wavelet transform of each component of the magnetic field time series is taken using $\omega_0 = 6$, with the relationship between wavelet scale and spacecraft frequency approximated as $f \approx \frac{\omega_0}{2\pi s} f_s$. A granular set of 19 scales ranging between ≈0.34 and ≈14.2 Hz is used to capture the dynamics of coherent transverse waves near ion scales. Figure 1 shows the wavelet transform scales with the integrated response, which is nearly uniform over the considered range of frequencies. At each wavelet scale, the local measurement of the mean magnetic field is computed corresponding to the Gaussian envelope of each wavelet scale,

$$B_{0j}(s, t) = \sum_{i=0}^{N-1} \left| \psi\left(\frac{t_i - \tau}{s}\right) \right| B_j(t_i), \tag{3}$$

where index j refers to the magnetic field component and $|\psi(\tau)| = \frac{A_s}{\pi^{1/4}} e^{-\frac{\tau^2}{2}}$, where A_s normalizes to unit energy (Horbury et al. 2008; Podesta 2009).

The vector wavelet transform in spacecraft coordinates $\boldsymbol{W}$ is then rotated into a field-aligned coordinate system $\hat{W} = (\hat{B}_{\perp 1}, \hat{B}_{\perp 2}, \hat{B}_0)$. The first perpendicular unit vector, $\hat{B}_{\perp 1}$, is computed as the cross product of the maximum variance direction of the mean field with the local mean field direction. The second unit vector, $\hat{B}_{\perp 2}$, ensures closure of a right-handed coordinate system $\hat{B}_{\perp 1} \times \hat{B}_{\perp 2} = \hat{B}_0$. To simplify notation, we use $B_{\perp 1}(f, t)$ and $B_{\perp 2}(f, t)$ to represent the complex valued wavelet transform of the magnetic field perpendicular to the mean direction, and $B_{\parallel}$ as the complex valued wavelet transform parallel to the mean field.

At each wavelet scale (frequency), quantities analogous to the Stokes parameters are defined between the perpendicular components of the wavelet transform:

$$S_0(f, t) = B_{\perp 1}^2 + B_{\perp 2}^2 \tag{4}$$

Table 1
Spacecraft Frame Polarization of Transverse Plasma Waves

Plasma Frame	Polarization (σ) $\boldsymbol{k}\cdot\boldsymbol{V}_{sw}>0$	$\boldsymbol{k}\cdot\boldsymbol{V}_{sw}<0$
Ion-resonant (+)	+	–
Electron-resonant (–)	–	+

Note. The apparent spacecraft polarization of resonant waves will invert when $\boldsymbol{k}\cdot\boldsymbol{V}_{sw}<0$. Assuming the Taylor hypothesis, $\boldsymbol{k}\cdot\boldsymbol{V}_{sw}>\omega(\boldsymbol{k})$, the observed spacecraft frame polarization of a wave with an intrinsic plasma-frame polarization depends on the sign of $\boldsymbol{k}\cdot\boldsymbol{V}_{sw}$.

$$S_1(f,t)=B_{\perp 1}^2-B_{\perp 2}^2 \tag{5}$$

$$S_2(f,t)=2\,\mathrm{Re}(B_{\perp 1}B_{\perp 2}^*) \tag{6}$$

$$S_3(f,t)=-2\,\mathrm{Im}(B_{\perp 1}B_{\perp 2}^*). \tag{7}$$

The quantity S_3 is associated with the magnetic helicity and circular polarization of the vector components $B_{\perp 1}$ and $B_{\perp 2}$ along $\boldsymbol{B}_0$ (Matthaeus & Goldstein 1982; Narita et al. 2009; Howes & Quataert 2010).

For a right-handed coordinate system, the vector $(\cos(\phi), \sin(\phi), B_0)$ with $B_0>0$, the phase convention of the Morlet wavelet in Equation (2), with S_3 defined in Equation (7), returns a normalized value $S_3/S_0=-1$. Physically, this polarization corresponds to the oscillation direction of electrons around the mean field in a stationary frame. The polarization corresponding to ion gyromotion is associated with $S_3/S_0=1$. The normalized fraction of circularly polarized power, $\sigma(f,t)$, is defined as a time average

$$\sigma(f,t)=\langle S_3\rangle/\langle S_0\rangle, \tag{8}$$

over two e-foldings of the Gaussian envelope of the Morlet wavelet, which reduces fluctuations in S_3 associated with stochastic turbulent fluctuations with an instantaneous polarization.

Instead of relying on a pseudovector convention of "left" and "right" handedness to describe helical fluctuations, we prefer the terms ion-resonant and electron-resonant polarization. These are unambiguous vectors defined relative to $\boldsymbol{B}_0$, and are intrinsic properties of the cold-plasma dispersion for parallel propagating electromagnetic waves: e.g., ICW resonate with ion gyromotion relative to $\boldsymbol{B}_0$ (Stix 1992; Gary 1993). Magnetic helicity is defined relative to the wave vector $\boldsymbol{k}$ such that, e.g., an ion-resonant wave has different values of helicity depending on its propagation direction (Narita et al. 2009). Due to single-point measurement effects, $\boldsymbol{k}$ in the solar wind frame is typically not directly determined, and the measured value of S_3 corresponds to the reduced magnetic helicity observed in the spacecraft frame (Matthaeus & Goldstein 1982; Howes & Quataert 2010). As noted by many authors, this degeneracy precludes a determination of the intrinsic plasma frame polarization of helical fluctuations. In contrast, the spacecraft frame polarization, defined relative to the background mean field, is directly measurable through the value of σ (Narita et al. 2009; Podesta & Gary 2011b; Klein et al. 2014). Table 1 provides an overview of the relationship between polarizations measured in the solar wind and spacecraft frames given the Doppler-shifted spacecraft frequency

$$2\pi f=\omega(\boldsymbol{k})+\boldsymbol{k}\cdot\boldsymbol{V}_{sw} \tag{9}$$

and assuming that the Taylor hypothesis $\boldsymbol{k}\cdot\boldsymbol{V}_{sw}\gg\omega(\boldsymbol{k})$ is applicable. The importance of this distinction is apparent in the subsequent sections.

3. Statistics of Wave Events

Figure 2(a)–(c) shows several long-duration coherent wave events spanning multiple wavelet scales on 2018 November 5. Signatures of mixed spacecraft frame polarization are evident in all three events. Assuming that all waves are of a single wave mode (intrinsic plasma frame polarization), the mixed spacecraft frame polarization at a single frequency indicates the presence of counter-propagating waves. The bottom panels show the power spectrum measured in each interval with the wavelet spectrum overlaid. Figure 2(d)–(f) demonstrates that a large fraction of the measured power at ion scales has a signature of circular polarization.

In addition to long-duration coherent events pictured in Figure 2, isolated solitary ion-scale waves are commonly observed over the encounter. Figure 3(a) shows an interval on 2018 November 5 with circularly polarized power that is significantly larger than the background ion-scale turbulence. A subset of the perpendicular power (i.e., S_0) from the day-long wavelet transform is presented in Figure 3(b), and the time-frequency spectrogram of σ in Figure 3(c); a set of hodograms of $B_{\perp 1}$ and $B_{\perp 2}$ at different wavelet scales is additionally presented.

In order to characterize the statistics of waves with coherent circular polarization, criteria were developed to separate intervals of wave power from the turbulent background. At each scale, intervals were identified as a wave event when $|\sigma|>0.7$, the event is extended continuously to neighboring times while $|\sigma|\geqslant 0.5$. The boundaries associated with $|\sigma|>0.7$ and $|\sigma|>0.5$ are shown in Figure 3(c). While multiple events at different frequencies (wavelet scales) may overlap in time, events at a given scale are necessarily separated from each other. For each event, the total power in the perpendicular fluctuations and duration of the event are measured

$$S_\sigma=\sum_{i=0}^{N_\sigma-1}S_{0i} \tag{10a}$$

$$T_\sigma=\sum_{i=0}^{N_\sigma-1}\Delta t_i, \tag{10b}$$

where the sum is over the N_σ indices between the start and end of each event given by the $|\sigma|>0.5$ threshold. Using this separation, the power spectral distributions of wave power can be determined, e.g., as in Figure 2(d)–(f).

3.1. Amplitude and Duration

During E1, 76,471 individual events (over all 19 scales) meeting the $|\sigma|>0.7$ threshold were automatically identified. Figure 4(a) shows the joint distribution of radial distance with root-mean-square (rms) wave amplitude, $B_\sigma=\sqrt{S_\sigma/N_\sigma}$. No significant dependence on radius was determined. Figure 4(b) shows the one-dimensional distribution of B_σ, which is peaked with rms wave amplitude of 4.23 nT. The distribution of fluctuation amplitude normalized to the mean field magnitude, B_σ/B_0, is shown in Figure 4(c), with the one-dimensional distribution with mean 0.04 shown in Figure 4(d). Though no

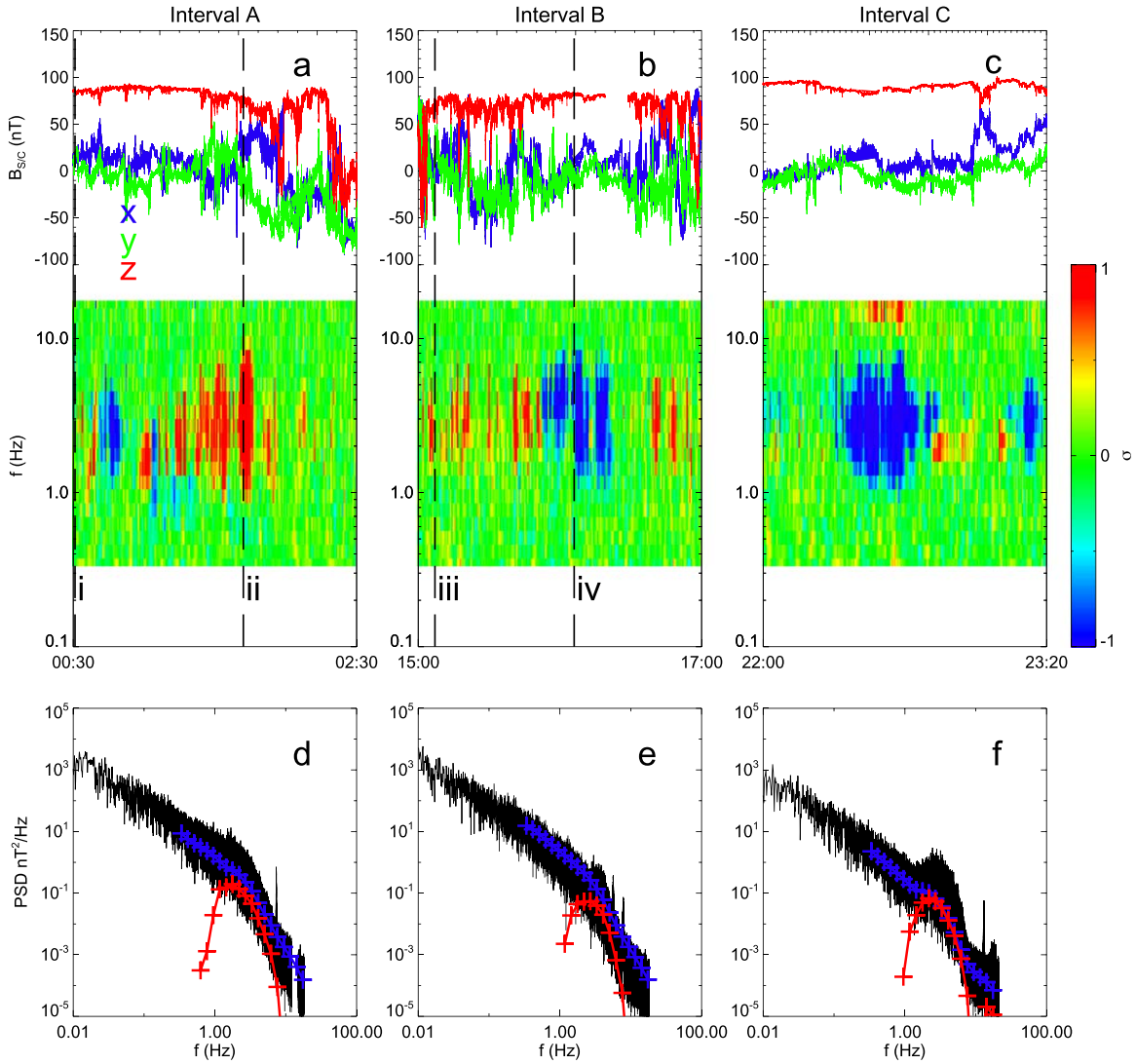

Figure 2. Panels (a)–(c) show time series for three long-duration circularly polarized wave storms on 2018 November 5, which dominate ion-scale turbulent fluctuations. Each panel shows $\sigma(f, t)$ the ratio between signed circularly polarized power to the total power of the perpendicular fluctuations (normalized reduced helicity). A value of $\sigma = -1$ (blue) corresponds to an electron resonant rotation relative to the mean field in the spacecraft frame. A value of $\sigma = 1$ (red) corresponds to ion-resonant polarization in the spacecraft frame (positive reduced magnetic helicity). Panels (d)–(f) show the trace power spectral densities $nT^2\ Hz^{-1}$ of the three intervals. Blue trace shows the corresponding wavelet power spectra $S_0(f)$ computed over each interval. Red trace shows the circular contribution to the power S_3. Dashed lines (i–iv) correspond to times of measured distribution functions shown in Figure 9.

dependence on radius is observed in B_σ, the scaling of $B_0 \sim r^{-2}$ does imply a trend in the normalized B_σ/B_0. At 35 $R_\odot$, the B_σ/B_0 distribution is peaked at $B_\sigma/B_0 = 0.05$, while the distribution at $50R_\odot$ occurs at $B_\sigma/B_0 = 0.08$. However, the variance of B_σ/B_0 at any given radius is on the order of the total radial variation.

Figure 4(e) shows the joint distribution of the event duration T_σ with distance. Figure 4(f) shows the distribution of event duration with a mean of 22 s. The longest event had a measured duration of 2968.4 s and an rms amplitude of 8.2 nT, which occurred with a mean field of 60.9 nT and a B_σ/B_0 of 0.13. The automated detection of circular polarization occasionally picks up fluctuations on the order of the mean field (e.g., $B_\sigma/B_0 \sim 1$), due to apparent instantaneous polarization of large-scale turbulent fluctuations; however, $B_\sigma/B_0 < 0.15$ for ~99% of measured events.

An estimate of the wave propagation direction is obtained using the angle between B_0 and the direction associated with the minimum variance direction (Sonnerup & Cahill 1967; Means 1972; Santolík et al. 2003; Jian et al. 2009).

Figure 4(g) shows the joint distribution of propagation angle with radius, demonstrating no discernible scaling with distance. Figure 4(h) shows the distribution of θ_{kB} between the propagation vector and the mean field with a mean angle of 9°.9 from the mean field; the median angle is 5°.3, and the distribution is peaked at $\theta_{kB} = 3°$. For a pure parallel propagating plane wave with 4 nT amplitude (16 nT^2 power), fluctuations with rms amplitude <1 nT are sufficient to introduce a perturbation to the minimum variance direction of this order. Accordingly, we cannot distinguish these waves from perfectly parallel propagating waves.

Figure 4(i) shows the distribution of event counts as a function of radial distance. While the occurrence of events is much higher at perihelion, the characteristics of the waves do not change drastically with distance. In all panels of Figure 4,

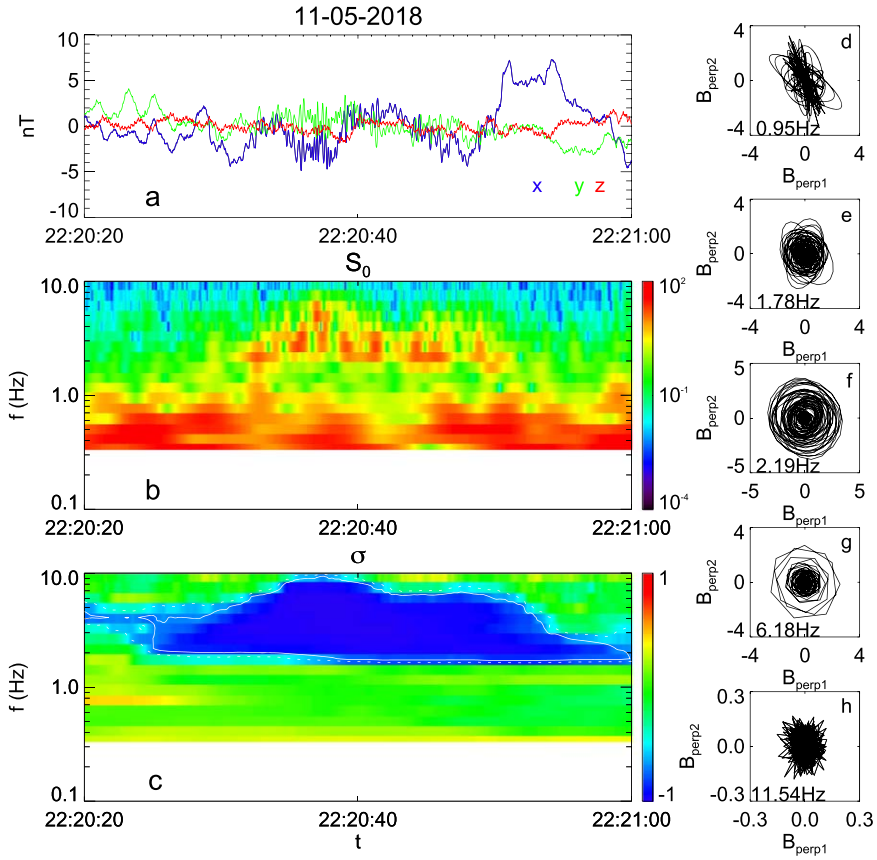

Figure 3. Example of an isolated wave event in background turbulence on 2018 November 5 at 22:20:40. (a) Magnetic field time series in spacecraft coordinates (mean subtracted). (b) Wavelet power spectrogram $S_0(t, f)$ for the interval; a broadband event is observed between 2 and 10 Hz, with negative polarization relative to the mean background field in the spacecraft frame. (c) Reduced helicity $\sigma = \langle S_3/S_0 \rangle \sim -1$ for the event, indicating an apparent electron resonant polarization. (d)–(h) Hodograms for $B_{\perp 1}$ and $B_{\perp 2}$ over a range of scales.

the distributions correspond to the total distribution of events measured at all 19 wavelet scales.

Contrasting the relative lack of scaling of measured wave properties, the background properties of the mean solar wind are measured with strong radial scalings. Bale et al. (2019) show that the mean background magnetic field has the expected r^{-2} scaling. The largest measured mean fields are on the order of 100 nT, while the smallest mean fields are on the order of 35 nT. Huang et al. (2019) measure the proton density to scale with $r^{-1.94}$ for the inbound phase of the encounter and a scaling of $r^{-2.44}$ for the outbound. Similarly, T_p is measured as $r^{-1.45}$ for the inbound and $r^{-0.90}$ encounter (see Huang et al. 2019). In any case, the radial scalings of background plasma parameters are not evident in the scaling of the measured wave parameters.

In Figure 4(b), (d) there is a secondary population with an approximate order of magnitude decrease in both amplitude (two orders in power) and duration. Because of the relative lower occurrence rate, and smaller characteristic amplitudes and durations, the presence of this secondary population should not severely impact the statistical analysis of the dominant ion-scale wave signatures. These events may either correspond to kinetic-scale turbulence with nonzero helicity measured at perpendicular angles to the mean field (e.g., Leamon et al. 1998; He et al. 2011; Podesta & Gary 2011a; Klein et al. 2014; Woodham et al. 2018), or residual signatures of narrowband reaction wheel noise (e.g., the Appendix).

3.2. Wave Frequencies and Ion Scales

For each wave interval, the spacecraft frequencies corresponding to the convected proton gyroscale, f_ρ, ion inertial scale, $f_{\rm di}$, and resonant cyclotron scale $f_{\rm res}$ are computed assuming Taylor hypothesis $2\pi\ f_{\rm sc} = \boldsymbol{k} \cdot V_{SW}$. The proton cyclotron frequency $f_{\rm ci}$ is additionally computed. The proton gyroscale is defined as

$$\rho = \frac{m_p V_{\perp \rm pth}}{qB_0},$$

while the inertial scale is related to the ion gyroscale by $d_p = \rho/\sqrt{\beta_\perp}$, where $\beta_\perp = V^2_{\perp \rm pth}/V^2_{\rm A}$ and the Alfvén speed is $V_{\rm A} = B_0/\sqrt{\rho_0 \mu_0}$. For protons moving along $\boldsymbol{B}_0$, the cyclotron resonance is given as

$$\Omega_p = \omega \pm k_\parallel V_{\rm th\parallel}, \tag{11}$$

where $\Omega_p = qB_0/m_p$, and the $\pm$ relates to the direction of the wave propagation relative to the particles motion (Woodham et al. 2018).

Using the parallel thermal speed from Huang et al. (2019) and the low-frequency limit for wave dispersion $\omega \sim k_\parallel V_{\rm A}$, e.g., Gary (1993), gives a resonance condition

$$k_\Omega = \frac{\Omega_p}{V_{\rm A} + V_{\parallel \rm pth}} \tag{12}$$

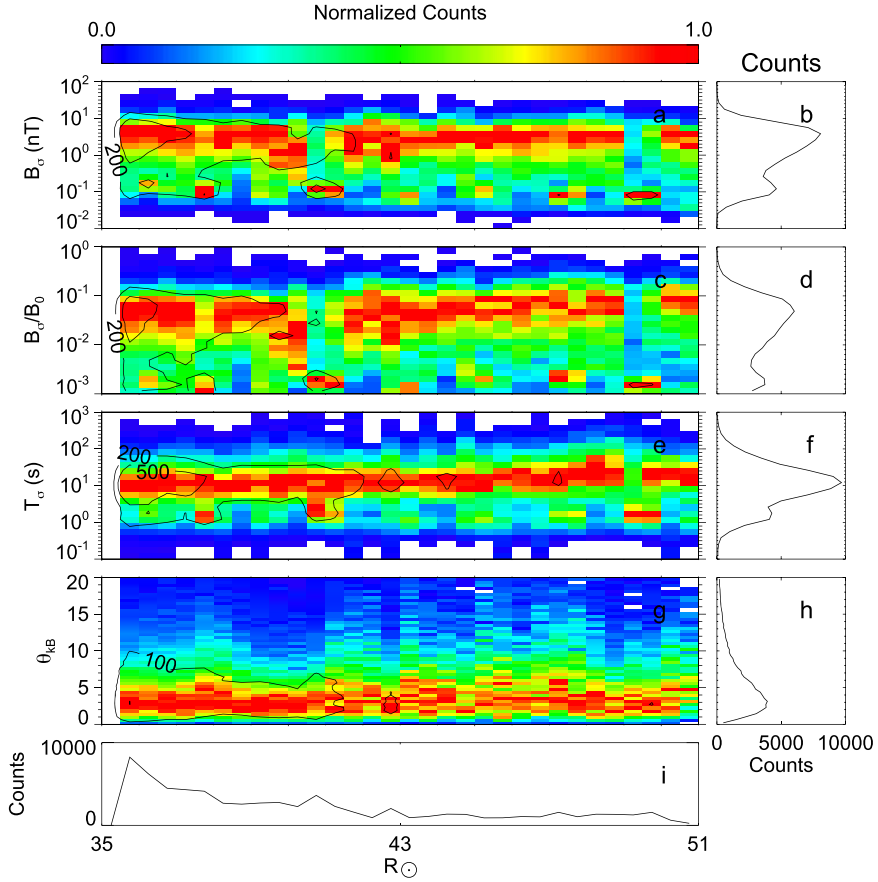

Figure 4. (a) Joint distribution of rms $B_\sigma = \sqrt{S_\sigma/N_\sigma}$ in nT for circularly polarized waves with $R_\odot$. The distribution is normalized to the most probable power at each radius. The average amplitude changes weakly with distance. (b) One-dimensional distribution of B_σ corresponding to an rms amplitude 4.22 nT. (c) Joint distribution of the normalized amplitude B_σ/B_0 with $R_\odot$ normalized to the most probable value at each radial radius. (d) One-dimensional distribution of B_σ/B_0, which has a mean of 0.04. (e) Joint distribution of average wave duration T_σ with $R_\odot$ normalized to the most probable duration at each radius. (f) One-dimensional distribution of T_σ, which has a mean of 21 s. (g) Joint distribution of circularly polarized wave propagation direction θ_{kB}, with $R_\odot$ normalized to most probable angle at each radius. (h) One-dimensional distribution of θ_{kB}, which has a mean of 5°. (i) One-dimensional distribution of counts with $R_\odot$, which monotonically decreases. Contours at 200 and 500 count levels are drawn over of the joint distributions (panels a, c, e, and g).

(Leamon et al. 1998; Woodham et al. 2019). Using the Taylor hypothesis, spacecraft frequencies corresponding to the Doppler-shifted gyroscale, inertial scale, and cyclotron resonant scale are given as

$$f_{\rm ci} = \frac{\Omega_p}{2\pi} = \frac{1}{2\pi}\frac{qB_0}{m_p} \tag{13a}$$

$$f_\rho = \frac{V_{\rm sw}}{2\pi}\frac{qB_0}{m_p V_{\perp \rm pth}} \tag{13b}$$

$$f_{\rm di} = \sqrt{\beta} f_\rho \tag{13c}$$

$$f_\Omega = \frac{V_{\rm sw}}{2\pi}\frac{\Omega_p}{V_{\rm A} + V_{\parallel \rm pth}}. \tag{13d}$$

Figure 5(a)–(d) shows the joint distribution of amplitude B_σ with wave frequency normalized to each of the frequencies in Equation (13). Figure 5(e)–(h) shows the corresponding distributions of event counts at each frequency, normalized to the three ion scales. Figure 5(a) shows that wave power occurs uniformly above $f_{\rm ci}$. Figure 5(b) shows that the wave power is peaked approximately near the Doppler-shifted resonant scale f_Ω in the spacecraft frame, while the power is cutoff at the Doppler-shifted gyroscale, f_ρ (Figure 5(d)). The intermediate ion inertial scale is Figure 5(c) is shown for completeness. The cutoff at f_ρ is consistent with Vlasov–Maxwell estimates of strong Alfvén damping ion-cyclotron at proton kinetic scales (Leamon et al. 1998; Gary 1999; Gary & Borovsky 2004).

Figure 5(c), (d) shows that a secondary population of events are present above the Doppler-shifted gyroscale, and these are consistent with the secondary population from Figure 4. However, we emphasize these events are separate from the distribution of ion-scale waves, and may be the result of statistical fluctuations, observations of KAW associated with nonzero helicity measured at perpendicular angles (e.g., He et al. 2011; Podesta & Gary 2011a; Woodham et al. 2018) or residual signatures of the narrowband reaction wheels (the Appendix).

3.3. Angular Dependence of Wave Occurrence and Energy

For each scale, the angular dependence of the total energy $S_0(f, \theta_{\rm BV})$ is computed by summing the energy for all times that $\theta_{\rm BV}$ was within range of angles $\theta_j < \theta_{\rm BV}$:

$$S_0(f, \theta_{\rm BV}) = \sum_{i=0}^{N-1} S_0(f, t_i | \theta_j < \theta_{\rm BV} < \theta_{j+1}). \tag{14}$$

The wave contribution to the total observed energy is computed as a function of angle $S_\sigma^T(f, \theta_{\rm BV})$ by summing the energy associated with coherent circularly polarized events,

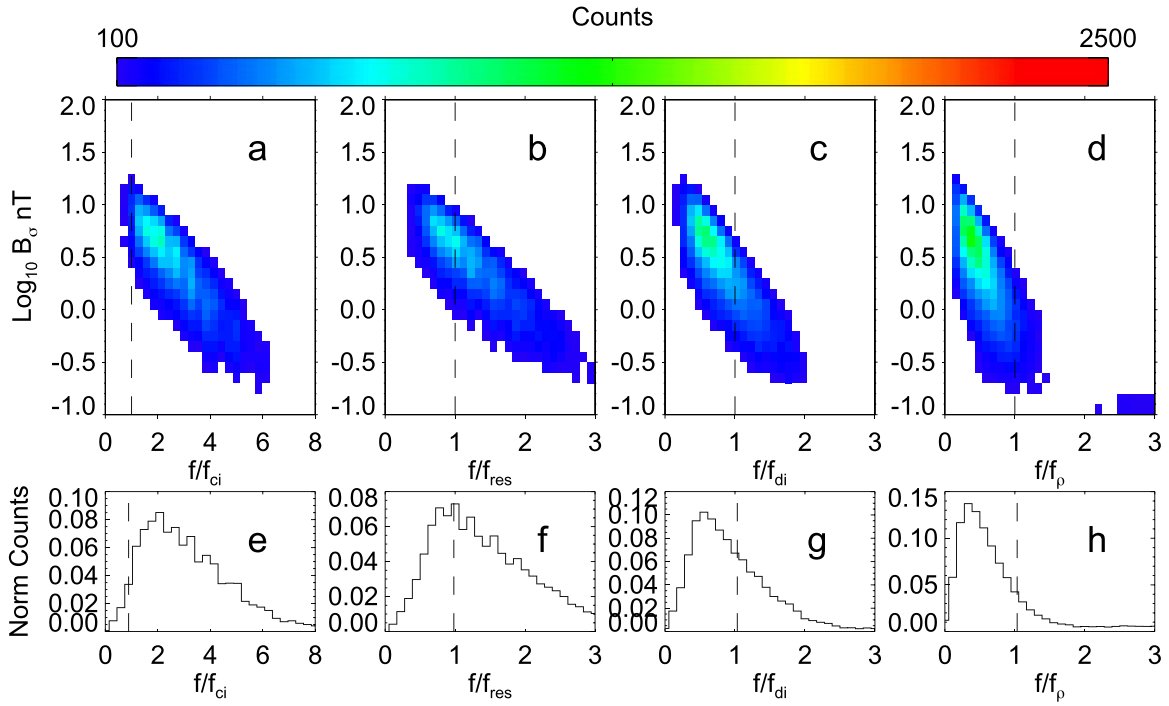

Figure 5. Panels (a)–(d) show a joint distribution of B_σ with the wave frequency normalized to spacecraft frequencies corresponding with the ion-cyclotron frequency and Doppler-shifted cyclotron-resonant scale, ion inertial length, and gyroradius: $f/f_{ci}, f/f_\Omega, f/f_d, f/f_\rho$. Panels (e)–(h) show measured distributions of $f/f_\Omega, f/f_d, f/f_\rho$. The power is peaked at frequencies corresponding to the cyclotron resonance ($f/f_{res} \sim 1$), and is cutoff at frequencies above the gyroscale ($f/f_\rho \sim 1$). Very few events are observed with $f/f_{ci} < 1$.

when θ_{BV} was within range of angles $\theta_j < \theta_{BV} < \theta_j + \Delta\theta$. The fraction of energy with positive (proton-resonant) and negative (electron-resonant) spacecraft frame polarization is further constrained by conditioning on the sign of σ:

$$S_\sigma^+(f, \theta_{BV}) = \sum_{k=0}^{N-1} S_\sigma(f, k|\theta_j < \theta_{BV} < \theta_{j+1}, \mathrm{sgn}(\sigma) = 1) \quad (15a)$$

$$S_\sigma^-(f, \theta_{BV}) = \sum_{k=0}^{N-1} S_\sigma(f, k|\theta_j < \theta_{BV} < \theta_{j+1}, \mathrm{sgn}(\sigma) = -1) \quad (15b)$$

$$S_\sigma^T(f, \theta_{BV}) = S_\sigma^+ + S_\sigma^-, \quad (15c)$$

where the sum k is an index over the set of events at frequency f is conditioned on the angle θ_{BV} and $|\sigma| > 0.7$ as defined in 2. The notation $\sum f(x|y)$ is understood as the sum of f, a function of x, conditioned on y.

The angular dependence of the occurrence of the ion-scale waves is obtained by comparing the integrated duration of the observed ion-scale waves with the angular distribution of θ_{BV}. The time distribution of θ_{BV} is measured as the the total time that $\theta_j < \theta_{BV} < \theta_j + \Delta\theta$, regardless of the polarization state:

$$T(f, \theta_{BV}) = \sum_{i=0}^{N-1} \Delta t(f|\theta_j < \theta_{BV} < \theta_{j+1}). \quad (16)$$

The wave occurrence rate as a function of scale and angle is determined by integrating the duration of waves, T_σ, that occur when θ_{BV} is within the angle bin $\theta_j + \Delta\theta_{BV}$.

$$T_\sigma^+(f, \theta_{BV}) = \sum_{k=0}^{N-1} T_\sigma(f, k|\theta_j < \theta_{BV} < \theta_{j+1}, \mathrm{sgn}(\sigma) = 1) \quad (17a)$$

$$T_\sigma^-(f, \theta_{BV}) = \sum_{k=0}^{N-1} T_\sigma(f, k|\theta_j < \theta_{BV} < \theta_{j+1}, \mathrm{sgn}(\sigma) = -1) \quad (17b)$$

$$T_\sigma^T(f, \theta_{BV}) = T_\sigma^+ + T_\sigma^-. \quad (17c)$$

The sum over i is taken over the time variable ($t_i = n_i \Delta t$) and the sum k over the index of wave events at a given scale.

Figure 6 shows normalized occurrence contours

$$T^\pm(f, \theta_{BV}) = T_\sigma^\pm(f, \theta_{BV})/T(f, \theta_{BV}) \quad (18)$$

for both positive and negative reduced helicity for each full day of perihelion 1 (2018 November 1–10). For each day, the median frequencies f_{ci} and f_ρ are computed and plotted. Contours in red show measured positive (apparent ion-resonant) polarization in the spacecraft frame, while contours in blue show a measured negative (apparent electron-resonant) polarization. The sign of the spacecraft frame polarization is calculated with respect to the mean field direction $\boldsymbol{B}_0(s, t)$ given in Equation (3). Waves propagating outward in the plasma frame are advected outward by the solar wind, such that measurements in the spacecraft frame are Doppler shifted to higher frequencies and the polarization is maintained in both frames. Conversely, sunward-propagating waves are advected outward by the solar wind, which Doppler shifts spacecraft measurements to lower frequencies. Given the ordering $V_{sw} > V_A$, a large Doppler shift through zero frequency will

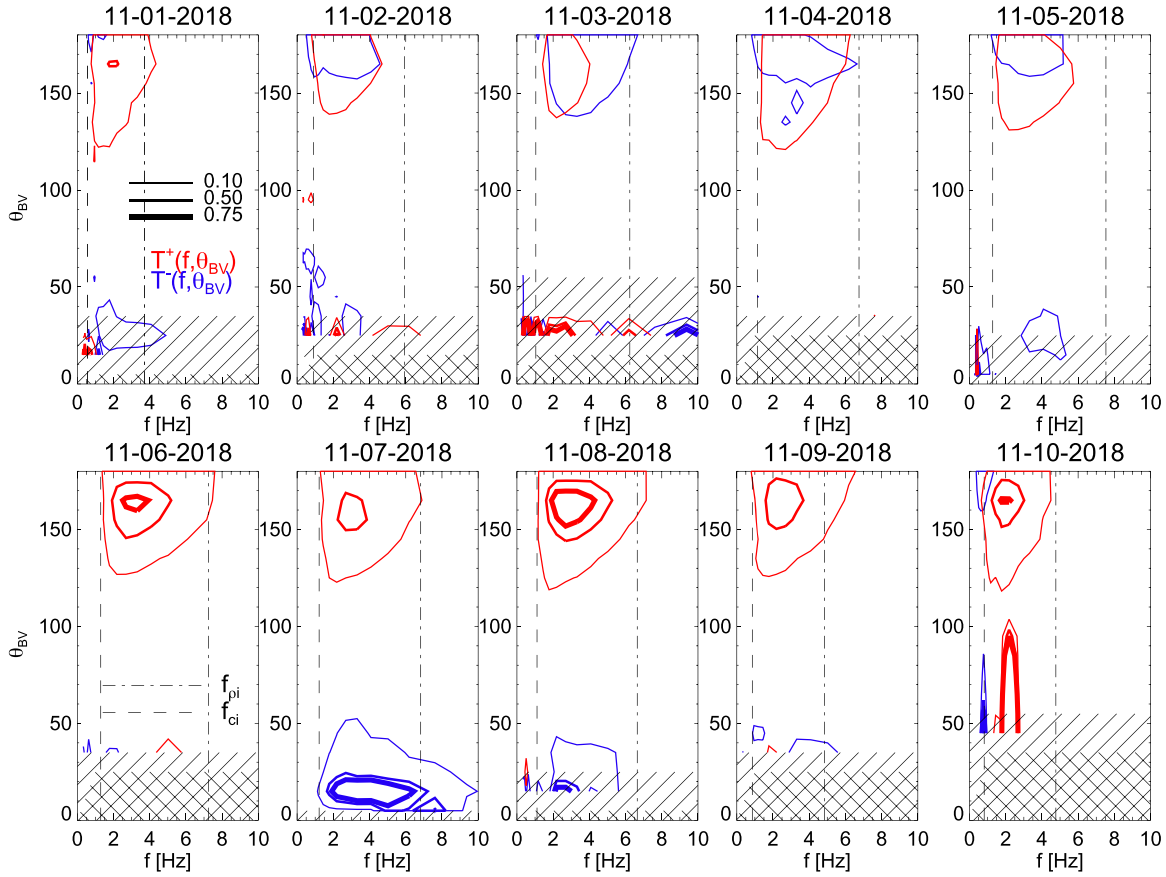

Figure 6. Normalized distribution of occurrence rates of circularly polarized coherent waves over $\theta_{\rm BV}$ and spacecraft frequency for each (full) day of *PSP* perihelion 1. Three levels of contours correspond to presence of waves in 10, 50, or 75% of intervals, with the angle between mean magnetic field and solar wind flow $\theta_j < \theta_{\rm BV} < \theta_{j+1}$, where $\theta_{j+1} - \theta_j = 10^\circ$. Red contours show occurrence of ion-resonant waves (positive helicity in spacecraft frame), and blue contours show occurrence rates of waves with apparent electron resonance (negative helicity in spacecraft frame). Sets of slanted hashes are used to identify angle bins accounting for <1% of the data for each day, and when no measurements in angle bin were made.

cause the inward-propagating plasma frame waves to appear with opposite polarization in the spacecraft frame (Narita et al. 2009; Howes & Quataert 2010; Podesta & Gary 2011b).

During the majority of the first encounter, *PSP* is connected to a coronal hole of negative polarity with a large-scale magnetic field pointing sunward, such that radial field intervals correspond to an angle of $\theta_{\rm BV} \sim 180^\circ$ (Bale et al. 2019; Badman et al. 2020). During radial field intervals, events with apparent positive and negative polarization each occur with $T_\sigma^\pm \sim 10 - 15\%$ of the time in a range of frequencies from ~1 to 5Hz. On the inbound phase, there is an equal distribution helical fluctuations with positive and negative polarization such that the total normalized occurrence rate at roughly antiparallel angles is $T_\sigma^T = T_\sigma^+ + T_\sigma^- \sim 20$–$30\%$. At perihelion (2018 November 6) and during the outbound portion of the orbit, increased occurrence rates are observed with $T_\sigma^T \sim 75\%$ when there is radial field alignment. On 2018 November 7, good statistics are obtained at parallel $\theta_{\rm BV}$, with strong negative reduced helicity evident for parallel field angles. The strong positive measurements at antiparallel $\theta_{\rm BV}$ and negative measurements at parallel $\theta_{\rm BV}$ suggest that the sign of the wave vector direction may change during the mean field reversal, such that $\boldsymbol{k} \cdot \boldsymbol{V}_{SW}$ changes sign and the apparent spacecraft polarization inverts. A similar inversion is observed in the MHD scale cross helicity during radial switchbacks of the mean magnetic field, as a change in direction of the Alfvénic flux with respect to a heliocentric coordinate system (Dudok de Wit et al. 2020; McManus et al. 2020). On 2018 November 8, there seems to be enhanced occurrence of wave events with $T^+ > 0.75$ at antiparallel $\theta_{\rm BV}$; such large occurrence rates are not evident in the inbound phase. In each case, there is cutoff at low frequencies aligned with the value $f_{\rm ci} = qB_0/2\pi m_p$. A high-frequency cutoff to the events is also observed. It increases to higher frequencies at lower altitudes, and likely corresponds to the advected gyroscale–e.g., Figure 5(a), (d).

Figure 7 shows normalized power rates $S_3^\pm/S_0$

$$S_3^\pm(f, \theta_{\rm BV}) = S_3^\pm(f, \theta_{\rm BV})/S_0(f, \theta_{\rm BV}) \tag{19}$$

for each day of E1.

Though events occur roughly 30–50% of the time, they contribute a significantly larger fraction to the total power ($S_\sigma^T = S_\sigma^+ + S_\sigma^- > 70\%$), indicating that the integrated contribution to the observed power is much larger than the contribution from background $k_\parallel$ turbulent fluctuations. The median $f_{\rm ci}$ and f_ρ for each day are again plotted. Intervals with a negative spacecraft frame polarization are commonly observed at higher frequencies than the positive polarization. Intuitively, for counter-propagating ion-resonant waves generated at the same wavenumber, Sunward-propagating waves are Doppler shifted to negative frequencies in the spacecraft frame, and thus should appear at lower frequencies and opposite helicity compared to the outward propagating waves, which are Doppler shifted to higher frequencies. Accordingly, if only ICW are present, then the observed distribution of polarizations

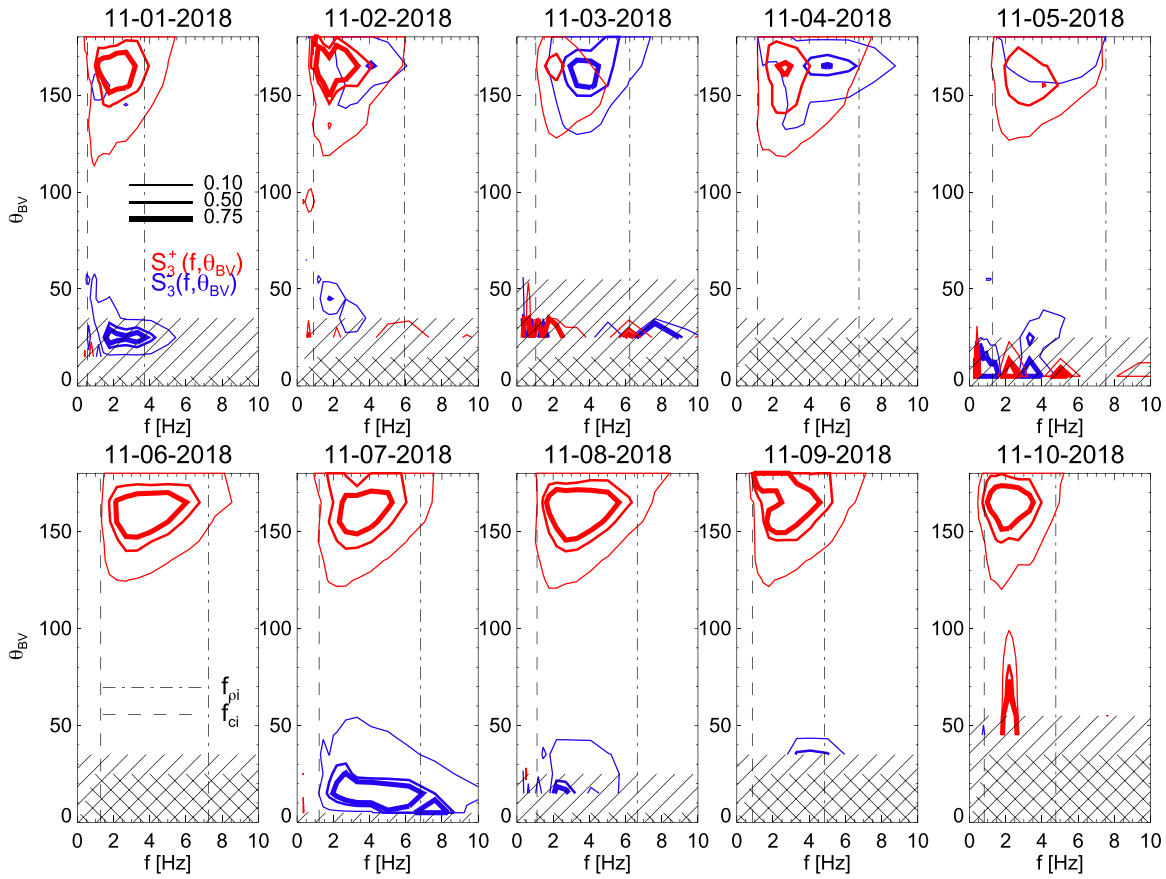

Figure 7. Distribution of energy in circularly polarized waves relative to total observed energy as a function of $\theta_{\rm BV}$ and spacecraft frequency for each (full) day of *PSP* perihelion 1. Three levels of contours correspond to the 10, 50, and 75% levels of fractional wave power relative to total measured energy when $\theta_j < \theta_{\rm BV} < \theta_{j+1}$, where $\theta_{j+1} - \theta_j = 10°$. Red contours show occurrence of polarization with apparent ion-resonance waves (positive helicity in spacecraft frame), and blue contours show occurrence rates of waves with apparent electron resonance (negative helicity in spacecraft frame). Sets of slanted hashed are used to identify angle bins accounting for <1% of the data for each day, and when no measurements in angle bin were made.

indicates that different wavenumbers may be excited for counter-propagating waves.

Observations of negative polarized waves at higher frequencies than positive polarized waves is additionally consistent with electron resonant waves propagating outward. However, it is not clear why the electron resonant waves would be peaked near ion cyclotron resonance, f_Ω, and cut off at the spacecraft frequency corresponding to the ion gyroscale f_ρ.

4. Observability of Parallel Propagating Waves in an Anisotropic Turbulent Cascade

Figures 6–7 reveal a statistical preference for the occurrence of circularly polarized waves during radial field intervals, a result consistent with observations of coherent waves at larger heliospheric distances (Murphy et al. 1995; Jian et al. 2009, 2014; Boardsen et al. 2015). However, this preference for radial field is possibly due to measurement effects. Observational evidence demonstrates that the anisotropy of solar wind turbulence leads to larger-amplitude fluctuations perpendicular to the mean magnetic field (Chen et al. 2010; Wicks et al. 2010; Horbury et al. 2012). The increased turbulent power at perpendicular angles may obscure waves with a coherent phase signature. Additionally, constraints imposed by single-point spacecraft measurements preclude a full vector measurement of the spectral density $P(\boldsymbol{k})$, such that quasi-parallel fluctuations may not be observable at oblique $\theta_{\rm BV}$.

To test these effects, we consider the reduced spectrum measured by a single spacecraft:

$$E(f, \theta_{\rm VB}) = \int d^3\boldsymbol{k} P(\boldsymbol{k}) \delta[2\pi f - (\boldsymbol{k} \cdot \boldsymbol{V}_{\rm sw} + \omega)] \qquad (20)$$

(Fredricks & Coroniti 1976).

The Taylor hypothesis corresponds to the limit $\boldsymbol{k} \cdot \boldsymbol{V}_{\rm sw} \gg \omega$. Similarly, the sign of the measured helical fluctuations corresponds to the reduced magnetic helicity measured along the sampling direction of the Doppler-shifted fluctuations in the spacecraft frame (Matthaeus & Goldstein 1982; Narita et al. 2009; Howes & Quataert 2010). Accordingly, observation of parallel propagating waves may be inhibited when the turbulent background fluctuations are sufficiently large (which is more likely to occur when sampling perpendicular cascade), or when the angle between the sampling direction and the mean magnetic field is sufficiently oblique that the polarization plane of the transverse waves is out of the plane defined by the reduced helicity.

A simple model spectrum is constructed to test the observability of parallel propagating waves at various angles of $\theta_{\rm BV}$ in the presence of an anisotropic turbulent background. The turbulence is modeled as a slab of parallel propagating ICW waves with a 2D background of axial symmetric

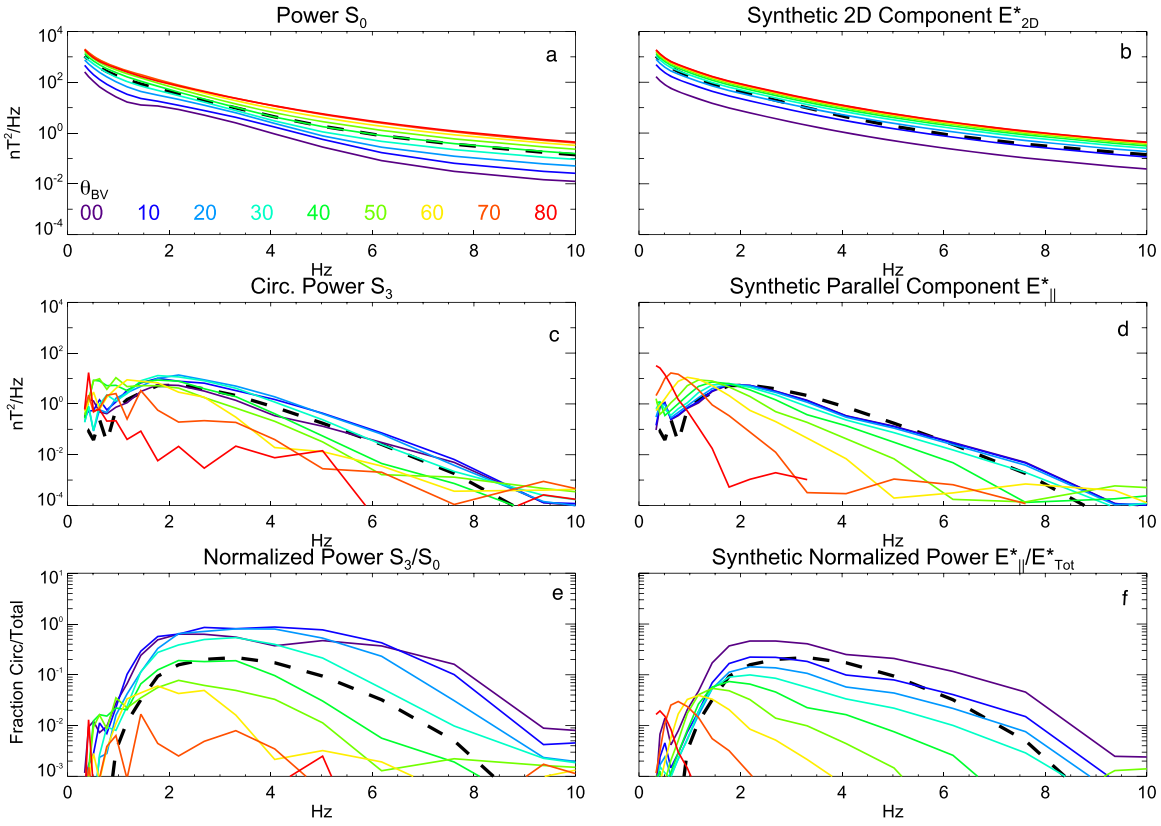

Figure 8. (a) Observations of reduced spectra on 2018 November 5 at various angles of θ_{BV}. (b) Synthetic two-dimensional component of background turbulent fluctuations assuming $k_\perp$ spectra at oblique angles, using observations of reduced spectra at $\theta_{BV} = 90°$. (c) Observations of reduced spectra at various θ_{BV} with significant circular polarization. (d) Synthesized component of circular polarized power at oblique θ_{BV}, using observations at $\theta_{BV} = 0°$ and an assumption of $k_\parallel$. (e) Fraction of circular power at various angles of θ_{BV}. (f) Fraction of circularly polarized power at various θ_{BV}, using the ratio of synthetic parallel and perpendicular spectra.

perpendicular turbulence

$$P(\boldsymbol{k}) = P_{2D}(k_\perp) + P_{ICW}(k_\parallel) \tag{21}$$

(Bieber et al. 1996). While in principle the contribution of either slab turbulence with $k_\perp = 0$, $k_\parallel \neq 0$, or a critically balanced turbulent spectrum $k_\perp \gg k_\parallel$, may be included, the observed dominance of the polarized wave power (Figure 7) suggests that this simplified model is sufficient.

The perpendicular turbulent spectrum is modeled as

$$P_{2D}(k_\perp) = A_{2D} k_\perp^{-(1+\alpha)} \delta(k_\parallel), \tag{22}$$

which, using Equation (20), gives a reduced spectrum

$$E_{2D}(f, \theta_{VB}) = C_{2D} f^{-\alpha} \sin\theta_{VB}^{\alpha-1}, \tag{23}$$

where A_{2D} and C_{2D} are constants and the Taylor hypothesis is assumed (Bieber et al. 1996; Horbury et al. 2008; Forman et al. 2011).

Observations of the turbulent spectrum at $\theta_{VB} \approx 90°$ constrain both the spectral index α and the coefficient C_{2D}, such that Equation (23) predicts the reduced turbulent spectrum at various θ_{BV} as

$$E^*_{2D}(f, \theta_{VB}) = E(f, 90°) \sin\theta_{BV}^{\alpha-1}. \tag{24}$$

Figure 8(a) shows the observed wavelet power spectra $S_0(f, \theta_{BV})$ on 2018 November 5. As expected, the perpendicular spectrum, $S_0(f, 80° < \theta_{BV} < 90°)$, demonstrates the largest power consistent with $k_\perp \gg k_\parallel$ anisotropy. Because of axial symmetry, the angular dependence of the power spectra is restricted to $0 < \theta_{BV} < 90°$, and the supplementary angle of θ_{BV} is used when $\theta_{BV} > 90$, in order to improve statistics.

Figure 8(b) shows synthetic turbulent power spectra $E^*_{2D}(f, \theta_{BV})$ for $\theta_{BV} < 90°$, using measurements of $S_0(f, 80° < \theta_{BV} < 90°)$ and Equation (24), with the empirically measured $\alpha = -1.9$.

By considering the effect of Equation (20) on a δ-function wave spectrum, we obtain the reduced spectrum associated with measuring narrowband quasi-parallel waves at oblique sampling angles:

$$P_{\delta\parallel}(k) = A_\parallel [\delta(k_{0\parallel} - k_\parallel)\delta(k_\perp)] \tag{25a}$$

$$E_{\delta\parallel}(f, \theta_{BV}) = \frac{A_\parallel}{V_{sw}\cos\theta_{BV}} \delta\left(k_{0\parallel} - \frac{2\pi f}{V_{sw}\cos\theta_{BV}}\right). \tag{25b}$$

Equation (25b) gives the reduced energy spectrum of a single wave mode wave-vector $\mathrm{k} = k_{0\parallel}\hat{B}_0$ as a function of spacecraft frequency and θ_{BV}; Figures 6–7 show that a broadband spectrum of parallel waves is typically observed. An estimate of the parallel spectrum of waves $P_\parallel(k_\parallel)$ is empirically constructed from observations of the contribution circularly polarized power to the wavelet spectrum when $0 < \theta_{VB} < 10°$ on 2018 November 5. Using $k_{0\parallel} \approx 2\pi f / V_{sw}$, the parallel spectrum is modeled as a superposition of weighted δ-functions at each wavelet scale

$$P_\parallel(k_\parallel) = \sum S^T_\sigma(f, 0)\delta(2\pi f / V_{sw} - k_\parallel). \tag{26}$$

A synthetic reduced spectrum at oblique θ_{VB} for the parallel ICW events $E_{\parallel}^{*}(f, \theta)$ observed at oblique angles is computed using Equation (25b) and the set of weighted δ functions to fit the parallel spectrum at $\theta_{BV} = 0$. Figure 8(c) shows the measured angular distribution of circularly polarized power at each frequency $S_{\sigma}^{T}(f, \theta_{BV})$. Figure 8(d) shows the synthetic reduced spectrum of circularly polarized power $E_{\parallel}^{*}(f, \theta)$ using $S_{\sigma}^{T}(f, 0)$ and Equation (25b).

Figure 8(e) shows the fractional polarized power of $S_{\sigma}^{T}(f, \theta_{BV})/S_0(f, \theta_{BV})$ measured on 2018 November 5. The corresponding ratio of synthetic reduced spectra $E_{\parallel}^{*}/E_{Tot}^{*}$, with $E_{Tot}^{*} = E_{\parallel}^{*} + E_{2D}^{*}$, is shown in Figure 8(f). A qualitatively similar evolution of the distribution of circularly polarized power is observed in both the observations and the synthetic reduced spectra, demonstrating that the disappearance of circular polarization signatures at oblique angles is consistent with sampling effect due to single point measurements of a quasi-parallel wave vector at oblique angles, as well as the increased amplitudes of the anisotropic turbulence. A similar phenomena has been recently studied by Hellinger et al. (2019), demonstrating that the generation of quasi-parallel coherent wave packets from the firehose instability in an expanding turbulent medium only appears in the one-dimensional power spectra at angles parallel to the mean field.

5. Comparison with Plasma Properties

Several authors have suggested that ion-scale waves observed at 1 au are driven by kinetic instabilities due to temperature anisotropies and beaming secondary proton and α particle populations (Jian et al. 2009; Podesta & Gary 2011b; Klein et al. 2014, 2018; Wicks et al. 2016; Woodham et al. 2019; Zhao et al. 2019). The SPC Faraday cup instrument on *PSP* measures a 1D (reduced) velocity distribution function in the Sun-pointing direction. Figures 9(a)–(d) shows four distribution functions from SPC corresponding to intervals in Figure 2; two Maxwellian fits are performed, corresponding to drifting proton distributions. Additionally, fits to α-particle distribution are shown in units of proton-equivalent speed (i.e., $\sqrt{2}$ times the proton speed due to the charge-to-mass ratio). Figure 9(a) shows the VDF at the beginning of the interval in Figure 2(a), where the fraction of circular power is low, while the distribution in Figure 9(b) corresponds to the circularly polarized cyclotron storm shown in Figure 2(a); the drift between two proton populations observed in Figure 9(b) may contribute to the growth of circularly polarized waves.

However, Figure 9(c) shows the measured VDF during an interval of low circular power taken from Interval B in Figure 2(b). Though some relative drift is observed between the populations, little polarized power is observed. Figure 9(d) shows the VDF of an interval with large circular polarization from Interval B in Figure 2(b) with smaller relative drift between proton populations, suggesting that the proton beam drift may not drive the distribution unstable in this event. However, there is a slight shift in the peak of the α-particle distribution, possibly indicating that streaming α-particles may contribute to these waves. Additionally, it is important to note that a single SPC measurement returns a reduced one-dimensional distribution and does not recover the full 3D distribution of the plasma, which may reveal large temperature anisotropies $T_{\perp}/T_{\parallel}$ in either the core or beam population commonly associated with electromagnetic ion cyclotron instabilities (Gary 1993; Podesta & Gary 2011b).

By integrating temperature observations from SWEAP/SPC and magnetic fields from FIELDS, Huang et al. (2019) estimate the proton temperature anisotropies in one-minute sampling intervals with a 10 s cadence. The normalized polarization $\sigma(f)$ is then computed for each 10 s integration for each wavelet scale. The largest positive value of $\sigma(f)^{+}$ is taken as a measure of ion-resonant waves, while the largest negative value $\sigma(f)^{-}$ is a measure of an electron-resonant polarization. Figures 10(a)–(b) shows joint probability distributions in the $\beta_{\parallel} - T_{\perp}/T_{\parallel}$ plane using the Huang et al. (2019) data set colored by $\sigma^{\pm}$. Contours in either plot show the distribution of measured wave events of the corresponding polarization. Additionally, instability thresholds for the Alfvén ion-cyclotron instability, $T_{\perp}/T_{\parallel} > 1$, and parallel firehose, which drives fast magnetosonic/whistlers at $T_{\perp}/T_{\parallel} < 1$, are drawn at $\gamma/\Omega_p = 10^{-2}$ and $\gamma/\Omega_p = 10^{-4}$ using fit parameters determined in Verscharen et al. (2016), consistent with growth rate contours in Hellinger et al. (2006). A statistical preference for ion-resonant polarization appears at $T_{\perp}/T_{\parallel} > 1$, and a secondary population of electron-resonant polarization appears at $T_{\perp}/T_{\parallel} < 1$, consistent with the results of Woodham et al. (2019) and Zhao et al. (2019) at 1 au. However, the distribution of measured ion-scale waves is not particularly bound into any region of the $\beta_{\parallel} - \mathrm{T}_{\perp}/T_{\parallel}$ plane. The presence of electron-resonant waves occurs at significantly lower values of β than what would be suggested by the fast magnetosonic/whistler waves driven by the firehose instability; mirror mode thresholds, which Huang et al. (2019) suggest bound the distribution of data, are additionally shown for completion (Hellinger et al. 2006; Verscharen et al. 2016). Further work is required to determine the effect of the secondary proton and α populations.

6. Independence from Electron-scale Waves

Malaspina et al. (2020) demonstrate that electrostatic waves near electron-cyclotron scales made by *PSP*/FIELDS occur preferentially during intervals with radial magnetic field. The occurrence of electron waves is parameterized by the electron wave counts per minute n_{elec}. In order to compare the occurrence of ion-scale wave events with high-frequency electron waves, the fractional circular power, $\bar{S}_3$, is computed on the same one-minute time base as the Malaspina et al. (2020) electron counts.

The probability of an ion-scale wave $P_{ion} = P(\bar{S}_3 \gg 0.05)$ is computed over the 10 day interval on the minute-cadence time base. Additionally, the probability of an electron wave count $P_{elec} = P(n_{elec} > 1)$ is determined. Individually, the probability of an ion wave event is $P_{ion} \sim 0.17$, and that of an electron event is $P_{elec} \sim 0.15$. The joint probability of observing both an ion-scale and electron-scale event is $P(n_{elec} > 1, \bar{S}_3 > 0.05) \approx 0.04$, which is approximately equal to the value of $P_{ion}P_{elec} = 0.03$, indicating a lack of correlation between the events. Additionally, when conditioning on radial intervals such that $\theta_{BV} < 25°$, the probabilities are

$$P_{ion}^{\parallel} = P(\bar{S}_3 > 0.05 | \theta_{BV} < 25°) = 0.38$$

$$P_{elec}^{\parallel} = P(n_{elec} > 1) | \theta_{BV} < 25°) = 0.35.$$

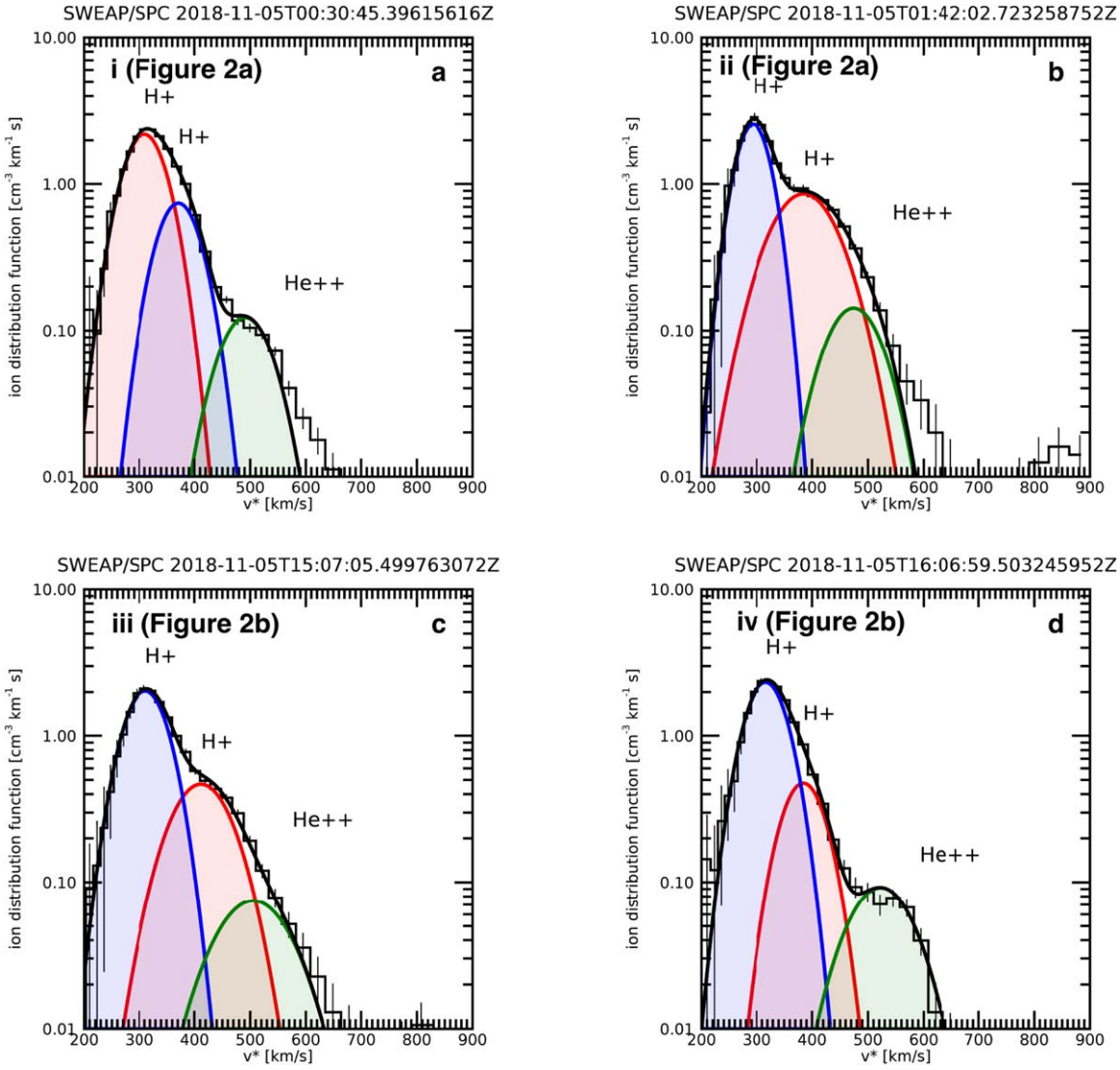

Figure 9. (a) SPC 1D velocity distribution function fit with two Maxwellian proton populations at a time with no circular polarization shown in Figure 2(a) (line i); the α-particle population is additionally fit to a Maxwellian and is shown at the proton equivalent speed, effectively shifting the peak speed by a factor of $\sqrt{2}$. (b) SPC 1-D velocity distribution function at time with significant coherent circular polarization shown in Figure 2(a) (line ii). (c) Velocity distribution function at time with no circular polarization shown in Figure 2(b) (line iii). (d) Velocity distribution function at time with significant coherent circular polarization circular polarization shown in Figure 2(b) (line iv).

However, the joint probability of both an electron wave count and a large ion-scale polarization is

$$P(n_{\rm elec}{>}1,\, \bar{S}_3 > 0.05)|\theta_{\rm BV} < 25^\circ) = 0.12,$$

which is approximately that of the probability

$$P^{\parallel}_{\rm ion} P^{\parallel}_{\rm elec} = 0.13$$

indicating uncorrelated distributions.

While both ion-scale and electron-scale waves have similar probabilities of occurrence, the joint distribution suggests that the occurrence of events is uncorrelated. Perhaps this result is not particularly surprising, as the ion instabilities that generate low-frequency waves at several Hz are likely decoupled from the electron instabilities acting at kHz; the independent occurrence of these waves reinforces that the young solar wind is subject to (and capable of maintaining) multiple instabilities, acting on different scales, which have in situ electromagnetic signatures.

7. Discussion

Circularly polarized ion-scale waves dominate $k_{\parallel}$ fluctuations in the inner heliosphere, and are likely a signature of processes connected to solar wind heating and acceleration through linear resonance and instabilities (Leamon et al. 1998; Hollweg & Isenberg 2002; Gary & Borovsky 2004; Wicks et al. 2016; Woodham et al. 2019; Zhao et al. 2019). Previously, Podesta & Gary (2011a) and He et al. (2011) identified signatures of magnetic helicity at parallel $\theta_{\rm BV}$ near ion scales without simultaneous identification of a separate (non-power-law) component in the observed spectra, suggesting the presence of low-level background quasi-parallel waves that interact with the turbulent cascade. In contrast, coherent

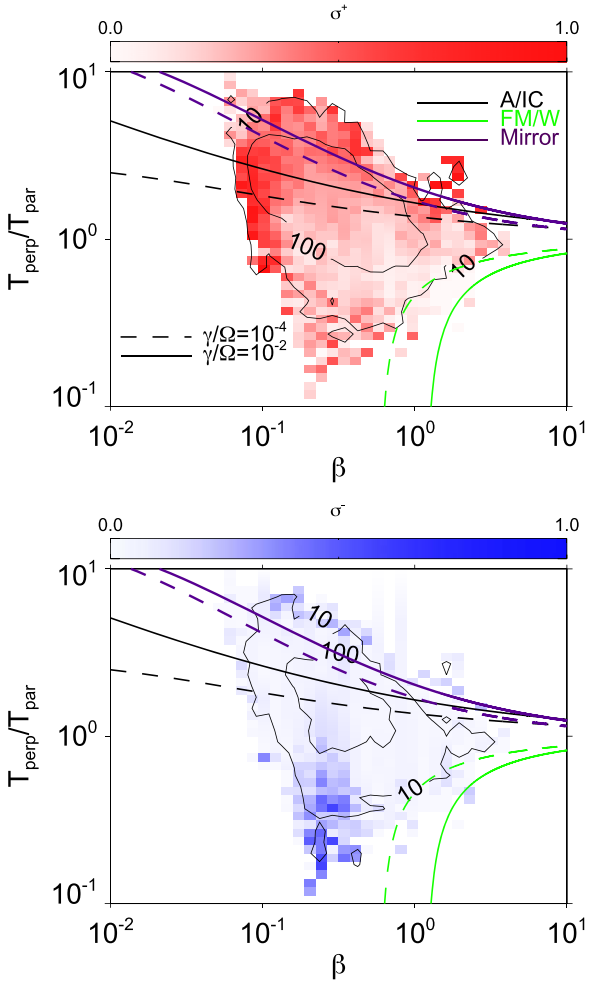

Figure 10. Distribution of encounter 1 measurements in $\beta_{\parallel}$-$T_{\perp}/T_{\parallel}$ plane. For each measurement, the maximum values of ion- and electron-resonant polarization ($\sigma^{\pm}$) are computed. (a) Data is colored by the mean (σ^{+}) for each measurement showing ion-resonant polarization. (b) Data is colored by the mean (σ^{-}) showing electron-resonant polarization. Contours show 10 and 100 count levels of the underlying distribution of measured waves. Alfvén/ion cyclotron (black) and fast-magnetosonic/whistler (green), and mirror (purple) instability thresholds are plotted at $\gamma/\Omega_p = 10^{-2}$ and $\gamma/\Omega_p = 10^{-4}$ levels from Verscharen et al. (2016).

waves have been thoroughly studied, with substantial evidence for generation through plasma instabilities (Podesta & Gary 2011b; Jian et al. 2014; Wicks et al. 2016; Telloni et al. 2019; Zhao et al. 2019).

While circularly polarized wave events are observed at 1 au (and elsewhere in the heliosphere), their occurrence is significantly enhanced in the inner heliosphere (Jian et al. 2009, 2010; Boardsen et al. 2015; Zhao et al. 2018). The statistical analysis of polarization signatures in Section 3.1 suggests that typical ion-scale waves have quasi-parallel wave numbers with rms amplitudes of ∼4 nT, which last on the order of 10 s to one minute—though the longest wave events maintain coherent circular polarization on hour-long timescales.

Section 3.2 shows that the observed waves are well-confined to spacecraft frame frequencies between the ion cyclotron frequency, $f_{ci} = qB_0/2\pi m$, and the Doppler-shifted proton-gyroscale, $f_{\rho} = \rho V_{sw}/2\pi$. Additionally, the measured distribution of waves is peaked at the spacecraft frequency corresponding to resonant ion-cyclotron interactions (Leamon et al. 1998; Woodham et al. 2018). The localization of waves to ion scales suggests that a large fraction of the waves are ion-resonant.

Section 3.3 demonstrates that circularly polarized waves occur in 30–50% of intervals with approximately radial mean magnetic field configurations. However, the analysis in Section 4 shows that the observability of these events is strongly dependent on the amplitude of the background turbulence and the angle θ_{BV}. The preferential occurrence of waves with a radial field alignment, though consistent with observations from the outer heliosphere, (e.g., Murphy et al. 1995; Jian et al. 2009; Boardsen et al. 2015), is consistent with sampling effects related to single point measurements of quasi-parallel waves in a quasi-perpendicular turbulent cascade. Recent work by Hellinger et al. (2019) has demonstrated this effect in models of expanding turbulent medium with coherent waves driven by the firehose instability. Accordingly, we cannot exclude the possibility that ion-scale waves are present during intervals with a nonradial magnetic field configuration. This result suggests that ion-scale waves with coherent circular polarization are possibly more common at 1 au than currently thought, as intervals of radial field are less frequently encountered at 1 au, due to the mean magnetic field direction along the Parker spiral.

Analysis of plasma distribution functions measured by SPC in Section 5 suggests that temperature anisotropy plays a role in the generation of ion-scale waves. Using measurements of the proton core temperature anisotropy by Huang et al. (2019), we find that ion-resonant fluctuations occur predominantly when the core proton temperature anisotropy $T_{\perp}/T_{\parallel} > 1$ and electron resonant fluctuations occur with $T_{\perp}/T_{\parallel} < 1$. This result is consistent with observations at 1 au by Woodham et al. (2019) and Zhao et al. (2019), and suggestive of generation of ICW events through Alfvén/ion cyclotron instability. However, the observed distribution of wave events of either polarization does not seem bounded by any portion of the $\beta - T_{\perp}/T_{\parallel}$ parameter space. This suggests that additional sources of free energy–e.g., beams and drifts–may be responsible for the growth and generation of these waves. A full analysis of beam and α-particle drifts is required to understand the generation of these events through instabilities. Our future work will incorporate the statistics of ion-scale waves with analysis of the full multipopulation 3D plasma distribution.

The events measured by *PSP* tend to have amplitudes ∼nT and do not scale strongly with radius. Due to the observed scaling in radial turbulent properties reported in Chen et al. (2020), these results suggest that the observed ion-scale waves have more in common with instability-driven events rather than an ambient quasi-parallel population of waves interacting with the background turbulence. However, the presence of an ambient population of cyclotron waves associated with the ion-cyclotron damping of the Alfvénic turbulent cascade is not ruled out by this study (Leamon et al. 1998; Woodham et al. 2018). Additionally, the lack of strong radial scaling suggests that the events are not signatures of near-Sun cyclotron heating, and instead are generated by in situ processes. This conjecture is additionally supported by the analysis in Section 3.2, which shows that wave power is peaked at local values of the cyclotron resonance and cut off above the local proton gyroscale, where strong cyclotron damping is expected (Leamon et al. 1998; Gary 1999). The weak dependence of

duration and amplitude with distance may suggest that the processes that generate the individual wave events do not vary greatly over 35–50$R_\odot$.

Observations of circularly polarized magnetic fluctuations in the spacecraft frame cannot uniquely determine the polarization in the solar-wind frame (Narita et al. 2009; Howes & Quataert 2010). An observed ion-resonant polarization in the spacecraft frame may be associated with either intrinsically ion-resonant waves propagating outward or inward-propagating electron waves that are Doppler-shifted in the spacecraft frame (He et al. 2011; Podesta & Gary 2011b; Klein et al. 2014; Roberts & Li 2015; Woodham et al. 2019). Conversely, observations of electron-polarized events correspond to outward-propagating electron-resonant modes or the Doppler shift of inward-propagating ion-resonant modes. A low-frequency cutoff observed at the proton-cyclotron frequency suggests that the waves may be outward-propagating fluctuations that are Doppler-shifted to higher frequencies in the spacecraft frame.

The Doppler shift of counter-propagating waves generated at the same plasma-frame wavenumber causes a frequency splitting of the waves in the spacecraft frame, with the inward-propagating waves occurring at lower frequencies. For a population of purely ion-resonant cyclotron waves, the inward-propagating waves appear at lower frequency and with an electron-resonant polarization. However, waves with electron-resonant helicity commonly appear at higher frequencies than the proton resonant helicity, e.g., Figure 7, 2018 November 3–4. This suggests that both ion-cyclotron and electron fast-magnetosonic/whistler waves may be present in these observations. Additionally, Figure 10 shows that there is a statistical preference for electron polarization with a $T_\parallel/T_\perp < 1$ and ion polarization for $T_\perp/T_\parallel > 1$. Future work to compare the observed polarization of electric field fluctuations simultaneously with magnetic fluctuations will provide a definitive measurement of the plasma-frame polarization of the observed waves (Santolík et al. 2003).

Though this work focuses on the dynamics of the protons, α particles and heavy ions can play a significant role shaping the dispersion of ion-scale waves (Hollweg & Isenberg 2002). Observations of the collisional processing of α particles at 1 au suggests that preferential ion heating may exist out to 20–40$R_\odot$, a range now explored by the *PSP* mission (Kasper et al. 2017). Understanding the effects of the full 3D drifting distribution function of protons and minor ions is imperative in determining the role of these waves in solar wind heating and acceleration.

8. Summary

Our results demonstrate the ubiquitous presence of ion-scale waves in the young solar wind. The waves are commonly found at scales coincident with proton-cyclotron resonance, and are cut off at the proton gyroscale. A weak radial scaling of the events is observed, indicating that events are likely generated through in situ processes. Analysis of core proton distribution functions suggests that temperature anisotropy may drive the waves, though we have not yet considered full distributions with drifting secondary proton and α populations.

Ion-scale waves are preferentially observed during alignment between the mean magnetic field and solar wind flow direction, consistent with observations further out in the heliosphere (Murphy et al. 1995; Jian et al. 2009, 2010, 2014). However an analysis of the reduced spectra associated with quasi-parallel waves made from single-point spacecraft measurements in an anisotropic turbulent background reveals that the disappearance of wave events at oblique angles is consistent with measurement effects. Accordingly, it is likely that polarized ion-scale waves driven by instabilities are present in the solar wind even during nonradial field intervals.

The FIELDS and SWEAP experiments on the Parker Solar Probe spacecraft were designed and developed under NASA contract NNN06AA01C. The authors acknowledge the extraordinary contributions of the *Parker Solar Probe* mission operations and spacecraft engineering teams at the Johns Hopkins University Applied Physics Laboratory. C.H.K.C. is supported by STFC Ernest Rutherford Fellowship ST/N003748/2. K.G.K. is supported by NASA ECIP grant 80NSSC19K0912.

Appendix
Reaction Wheels

The *PSP* spacecraft is outfitted with four reaction wheels that, while necessary for maintaining stable on-orbit pointing, contribute a considerable amount of large-amplitude coherent noise to the FIELDS observations. The wheels rotate at frequencies ranging from less than 1 Hz to several tens of Hz. Rotation is often coupled with multiple wheels rotating at (or very near) the same frequency and drifting together over time, though each wheel is in principle capable of rotating at a unique frequency. Each wheel generates a magnetic signature at its rotation frequency, which is easily observable in both survey and burst-mode data from the FIELDS magnetometers. Though the wheels are confined to a range of rotation frequencies, harmonics and beating between wheels is observable as narrowband noise at much higher frequencies. Additionally, autonomous spacecraft thruster firings are used to ensure that the momentum of the spacecraft stays within orbital requirements, allowing for the reaction wheels to rapidly change rotation rates without endangering spacecraft pointing. During the first encounter, a single autonomous firing occurred on 2018 November 6 around 08:26.

The large-amplitude coherent signals generated by the spacecraft reaction wheels—as visible, e.g., in the bottom panels of Figure 2—may contaminate measurements sensitive to polarization of the environmental signal. Figure 11(a) shows a spectrogram from 2018 November 1 computed using a short-time Fourier transform; narrowband features are observed in the spectrogram corresponding to the wheel rotation frequencies. Preprocessing and denoising of the FIELDS data may be required in studies that are sensitive to reaction wheel signatures. While this appendix demonstrates one technique to address contamination from reaction wheels, in principle, tailored methods should be used on a case-by-case basis in order to minimize effects from artifacts resulting from data processing.

Reaction wheel rotation rates inherently drift in order to ensure stable pointing of the spacecraft. Typical drift rates are on the order of Hz per day. However, over sufficiently short time intervals, the drift of the wheel frequencies is negligible, such that electromagnetic contamination is confined to a finite, narrowband range of frequencies. In order to remove the reaction wheel signals, a narrowband notch filter is used to

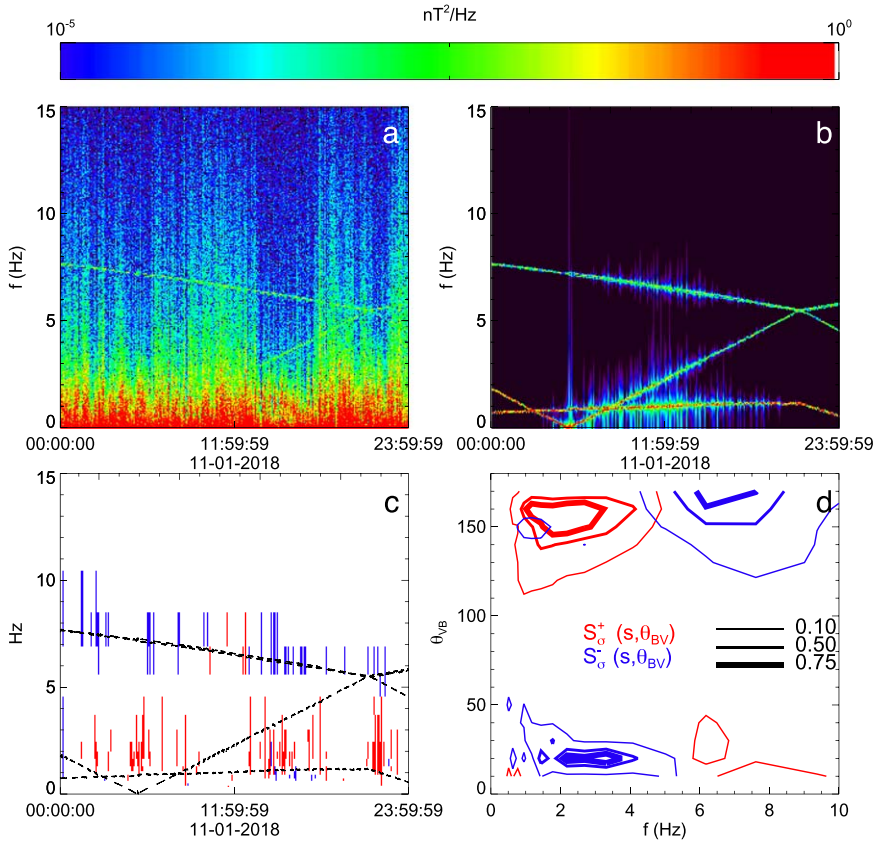

Figure 11. (a) Short-time Fourier spectrogram of the x-axis magnetic field on 2018 November 1. (b) Short-time Fourier spectrogram of the x-axis magnetic field on 2018 November 1 when retaining only frequencies contaminated by reactions wheels. (c) Intervals with negative reduced helicity corresponding to apparent electron resonant polarization (blue) and positive reduced helicity corresponding to an apparent ion resonant polarization (red). (d) Distribution of $S^{\pm}$ circularly polarized power in plane of f and$\theta_{\rm BV}$ when reaction wheel signatures are not removed; compare to Figure 7.

attenuate power at each of the wheel rotation frequencies $f_{\rm wj}$ in the Fourier domain. For an interval $N\Delta t$, the frequency resolution of the Fourier transform is $\Delta f = f_s/N$, where $f_s = 1/\Delta t$. The drifting wheel frequencies are confined to a narrow range of spectral bins by choosing a sample length N, which confines the drifting wheel power to a single bin Δf. The rate of change of the wheel frequencies, $df_{\rm wj}/dt$, is measured from spacecraft house keeping data. The sample size N is chosen such that the maximum rate of change of the wheel frequency over N corresponds roughly to the frequency resolution Δf.

$$\left.\frac{df_w}{dt}\right|_{\rm max} N\Delta t = \frac{f_s}{N}$$

$$N = \sqrt{\frac{f_s}{(df_w/dt)\,\Delta t}}.$$

For each N samples, the magnetic field is Fourier transformed; coefficients corresponding to the contaminated frequencies ($f_{\rm wj}$) are attenuated by -80 dB and the inverse Fourier transform is taken. In practice, each day of down-sampled data has a total number of samples of $N_T = 3164{,}060$ samples, where the factor of N_T closest to N is chosen as the sample length. For 2018 November 1, $N = 1124$ samples (approximately $\sim$30 s). A processed time series is then given as the reconstructed set of $M = N_T/N$ intervals.

Figure 11(b) shows the spectrogram of 2018 November 1 when only frequencies associated with $f_{\rm wj}$ are kept. Figure 11(c) shows the indices of $|\sigma| = |<S_3/S_0>| > 0.7$ computed from the wavelet transform in Section 3; the reaction wheel frequencies are shown as dashed lines. Positive σ is shown in red, and negative σ shown in blue. A signature of circular polarization follows one of the drifting reaction wheels over the day between 6 and 8 Hz. The spectral power in these frequencies is commonly dominated by the narrowband spectral line, suggesting that observation of polarization in these frequencies is likely due to contamination by the reaction wheel. Around mid-day, the polarization flips, but this is likely due to the definition of polarization with respect to the local mean field; this is consistent with the inversion of handedness at frequencies greater than 5 Hz is seen in Figure 11(c).

The reaction wheel signal contributes polarized power that can be misidentified in statistical surveys of coherent power. For example, when computing the fractional power in frequency with $\theta_{\rm BV}$, a strong signature of negative σ is observed at frequencies greater than 5 Hz, similar to the circularly polarized wave events. However, after processing out frequencies with reaction wheels, this feature is no longer present (e.g., the 2018 November 1 panel shown in Figure 7).

The primary goal of this processing method is to remove narrowband power with strong polarization signatures that contaminate the wavelet transform of the magnetic field observations. The large wavelet bandwidth (in comparison to the narrowband wheel signature) acts to average the spectral components near the central frequency of each wavelet scale. When power from a reaction wheel is present within a

wavelet's bandwidth, the wavelet response to the reaction wheel signature may dominate, resulting in a contaminated measurement. By attenuating the reaction wheel signal, the wavelet response captures the average power and phase of the noncontaminated frequencies near its central frequency.

The authors considered restricting the study to only wave events that were localized from reaction wheel signatures. In essence, an alternative approach to controlling for reaction wheels effects is to avoid any data processing, and to simply remove coherent features occurring near contaminated frequencies from the ensemble of events. However, many wave events with frequencies near contaminated frequencies have enough power that the electromagnetic signature from the reaction wheel negligible–i.e., the wave rms amplitudes are commonly of order nT versus the reaction wheel amplitudes at a fraction of a nT. It is thus preferable to remove the narrowband power at the contaminated frequencies and let the wavelet respond to the remaining power in nearby frequencies, rather than simply removing all events that have the possibility of contamination from the catalog of observed events.

The discrete joining individually processed intervals, which inevitably introduces artifacts in the time series: specifically, small discontinuities will exist at the edge of each processed interval. These discontinuities predominantly affect the high end of the signal bandwidth near the Nyquist (∼18 Hz). The fraction of power removed at each time is a small fraction of the total observed power, such that discontinuities do not drastically change the structure of the magnetic field measurements. However, some measures of the magnetic field, e.g., increment-based analyses commonly used to study solar wind turbulence, will certainly be sensitive to these discontinuities, and alternative methods of compensating for reaction wheels will be required.

ORCID iDs

Trevor A. Bowen https://orcid.org/0000-0002-4625-3332
Jia Huang https://orcid.org/0000-0002-9954-4707
Kristopher G. Klein https://orcid.org/0000-0001-6038-1923
David M. Malaspina https://orcid.org/0000-0003-1191-1558
Michael Stevens https://orcid.org/0000-0002-7728-0085
Stuart D. Bale https://orcid.org/0000-0002-1989-3596
J. W. Bonnell https://orcid.org/0000-0002-0675-7907
Anthony W. Case https://orcid.org/0000-0002-3520-4041
Benjamin D. G. Chandran https://orcid.org/0000-0003-4177-3328
C. C. Chaston https://orcid.org/0000-0002-0029-717X
Christopher H. K. Chen https://orcid.org/0000-0003-4529-3620
Thierry Dudok de Wit https://orcid.org/0000-0002-4401-0943
Keith Goetz https://orcid.org/0000-0003-0420-3633
Peter R. Harvey https://orcid.org/0000-0002-6938-0166
Gregory G. Howes https://orcid.org/0000-0003-1749-2665
J. C. Kasper https://orcid.org/0000-0002-7077-930X
Kelly E. Korreck https://orcid.org/0000-0001-6095-2490
Robert J. MacDowall https://orcid.org/0000-0003-3112-4201
Michael D. McManus https://orcid.org/0000-0001-6077-4145
Marc Pulupa https://orcid.org/0000-0002-1573-7457
Phyllis Whittlesey https://orcid.org/0000-0002-7287-5098

References

Badman, S. T., Bale, S. D., Martínez Oliveros, J. C., et al. 2020, ApJS, doi:10.3847/1538-4365/ab4da7
Bale, S. D., Badman, S. T., Bonnell, J. W., et al. 2019, Natur, 576, 237
Bale, S. D., Goetz, K., Harvey, P. R., et al. 2016, SSRv, 204, 49
Bieber, J. W., Wanner, W., & Matthaeus, W. H. 1996, JGR, 101, 2511
Boardsen, S. A., Jian, L. K., Raines, J. L., et al. 2015, JGRA, 120, 10207
Brain, D. A., Bagenal, F., Acuña, M. H., et al. 2002, JGRA, 107, 1076
Case, A. C., Kasper, J. C., Stevens, M. L., et al. 2020, ApJS, doi:10.3847/1538-4365/ab5a7b
Chandran, B. D. G., Verscharen, D., Quataert, E., et al. 2013, ApJ, 776, 45
Chen, C. H. K., Bale, S. D., Bonnell, J. W., et al. 2020, ApJS, doi:10.3847/1538-4365/ab60a3
Chen, C. H. K., Wicks, R. T., Horbury, T. S., et al. 2010, ApJL, 711, L79
Cranmer, S. R. 2000, ApJ, 532, 1197
Cranmer, S. R. 2014, ApJS, 213, 16
Cranmer, S. R., Field, G. B., & Kohl, J. L. 1999, ApJ, 518, 937
Delva, M., Mazelle, C., Bertucci, C., et al. 2011, JGRA, 116, A02318
Dudok de Wit, T., Alexandrova, O., Furno, I., et al. 2013, SSRv, 178, 665
Dudok de Wit, T., Krasnoselskikh, V. V., Bale, S. D., et al. 2020, ApJS, doi:10.3847/1538-4365/ab5853
Farge, M. 1992, AnRFM, 24, 395
Forman, M. A., Wicks, R. T., & Horbury, T. S. 2011, ApJ, 733, 76
Fox, N. J., Velli, M. C., Bale, S. D., et al. 2016, SSRv, 204, 7
Fredricks, R. W., & Coroniti, F. V. 1976, JGR, 81, 5591
Gary, S. P. 1993, Theory of Space Plasma Microinstabilities (Cambridge: Cambridge Univ. Press)
Gary, S. P. 1999, JGR, 104, 6759
Gary, S. P., & Borovsky, J. E. 2004, JGRA, 109, A06105
Gary, S. P., Skoug, R. M., Steinberg, J. T., et al. 2001, GeoRL, 28, 2759
He, J., Marsch, E., Tu, C., et al. 2011, ApJ, 731, 85
Hellinger, P., Matteini, L., Landi, S., et al. 2019, ApJ, 883, 178
Hellinger, P., Trávníček, P., Kasper, J. C., et al. 2006, GeoRL, 33, L09101
Hollweg, J. V. 1974, JGR, 79, 1539
Hollweg, J. V., & Isenberg, P. A. 2002, JGRA, 107, 1147
Hollweg, J. V., & Johnson, W. 1988, JGR, 93, 9547
Horbury, T. S., Forman, M., & Oughton, S. 2008, PhRvL, 101, 175005
Horbury, T. S., Wicks, R. T., & Chen, C. H. K. 2012, SSRv, 172, 325
Howes, G. G., & Quataert, E. 2010, ApJL, 709, L49
Huang, J., Kasper, J. C., Vech, D., et al. 2019, arXiv:1912.03871
Isenberg, P. A. 1984, JGR, 89, 2133
Isenberg, P. A. 1990, JGR, 95, 6437
Isenberg, P. A., & Hollweg, J. V. 1983, JGR, 88, 3923
Jian, L. K., Russell, C. T., Luhmann, J. G., et al. 2009, ApJL, 701, L105
Jian, L. K., Russell, C. T., Luhmann, J. G., et al. 2010, JGRA, 115, A12115
Jian, L. K., Wei, H. Y., Russell, C. T., et al. 2014, ApJ, 786, 123
Kasper, J. C., Abiad, R., Austin, G., et al. 2016, SSRv, 204, 131
Kasper, J. C., Klein, K. G., Weber, T., et al. 2017, ApJ, 849, 126
Kasper, J. C., Lazarus, A. J., & Gary, S. P. 2002, GeoRL, 29, 1839
Kasper, J. C., Maruca, B. A., Stevens, M. L., et al. 2013, PhRvL, 110, 091102
Kivelson, M. G., Khurana, K. K., Walker, R. J., et al. 1996, Sci, 274, 396
Klein, K. G., Alterman, B. L., Stevens, M. L., et al. 2018, PhRvL, 120, 205102
Klein, K. G., Howes, G. G., TenBarge, J. M., et al. 2014, ApJ, 785, 138
Kohl, J. L., Noci, G., Antonucci, E., et al. 1997, SoPh, 175, 613
Kohl, J. L., Noci, G., Antonucci, E., et al. 1998, ApJL, 501, L127
Leamon, R. J., Smith, C. W., Ness, N. F., et al. 1998, JGR, 103, 4775
Malaspina, D. M., Halekas, J., Berčič, L., et al. 2020, ApJS, doi:10.3847/1538-4365/ab4c3b
Marsch, E. 2012, SSRv, 172, 23
Marsch, E., Schwenn, R., Rosenbauer, H., et al. 1982, JGR, 87, 52
Matthaeus, W. H., & Goldstein, M. L. 1982, JGR, 87, 6011
McManus, M. D., Bowen, T. A., Mallet, A., et al. 2020, ApJS, doi:10.3847/1538-4365/ab6dce
Means, J. D. 1972, JGR, 77, 5551
Murphy, N., Smith, E. J., Tsurutani, B. T., et al. 1995, SSRv, 72, 447
Narita, Y., Kleindienst, G., & Glassmeier, K.-H. 2009, AnGeo, 27, 3967
Podesta, J. J. 2009, ApJ, 698, 986
Podesta, J. J., & Gary, S. P. 2011a, ApJ, 734, 15
Podesta, J. J., & Gary, S. P. 2011b, ApJ, 742, 41
Roberts, O. W., & Li, X. 2015, ApJ, 802, 1
Russell, C. T., Luhmann, J. G., Schwingenschuh, K., Riedler, W., & Yeroshenko, Y. 1990, GeoRL, 17, 897
Santolík, O., Parrot, M., & Lefeuvre, F. 2003, RaSc, 38, 1010
Sonnerup, B. U. O., & Cahill, L. J. 1967, JGR, 72, 171
Stix, T. H. 1992, Waves in Plasmas (Melville, NY: AIP)

Telloni, D., Carbone, F., Bruno, R., et al. 2019, ApJL, 885, L5
Torrence, C., & Compo, G. P. 1998, BAMS, 79, 61
Tsurutani, B. T., Arballo, J. K., Mok, J., et al. 1994, GeoRL, 21, 633
Tu, C.-Y., & Marsch, E. 1997, SoPh, 171, 363
Verscharen, D., Chandran, B. D. G., Klein, K. G., et al. 2016, ApJ, 831, 128
Verscharen, D., Klein, K. G., & Maruca, B. A. 2019, LRSP, 16, 5
Wicks, R. T., Alexander, R. L., Stevens, M., et al. 2016, ApJ, 819, 6
Wicks, R. T., Horbury, T. S., Chen, C. H. K., et al. 2010, MNRAS, 407, L31
Wilson, L. B., Stevens, M. L., Kasper, J. C., et al. 2018, ApJS, 236, 41
Woodham, L. D., Wicks, R. T., Verscharen, D., et al. 2018, ApJ, 856, 49
Woodham, L. D., Wicks, R. T., Verscharen, D., et al. 2019, ApJL, 884, L53
Yoon, P. H. 2017, RvMPP, 1, 4
Zhao, G. Q., Feng, H. Q., Wu, D. J., et al. 2018, JGRA, 123, 1715
Zhao, G. Q., Feng, H. Q., Wu, D. J., et al. 2019, ApJ, 871, 175